# The RNA-binding protein Musashi controls axon compartment-specific synaptic connectivity through ptp69D mRNA poly(A)-tailing

Landínez-Macías, María ; Qi, Weihong ; Bratus-Neuenschwander, Anna ; Müller, Martin ; Urwyler, Olivier

Abstract: Synaptic targeting with subcellular specificity is essential for neural circuit assembly. Developing neurons use mechanisms to curb promiscuous synaptic connections and to direct synapse formation to defined subcellular compartments. How this selectivity is achieved molecularly remains enigmatic. Here, we discover a link between mRNA poly(A)-tailing and axon collateral branch-specific synaptic connectivity within the CNS. We reveal that the RNA-binding protein Musashi binds to the mRNA encoding the receptor protein tyrosine phosphatase Ptp69D, thereby increasing poly(A) tail length and Ptp69D protein levels. This regulation specifically promotes synaptic connectivity in one axon collateral characterized by a high degree of arborization and strong synaptogenic potential. In a different compartment of the same axon, Musashi prevents ectopic synaptogenesis, revealing antagonistic, compartment-specific functions. Moreover, Musashi-dependent Ptp69D regulation controls synaptic connectivity in the olfactory circuit. Thus, Musashi differentially shapes synaptic connectivity at the level of individual subcellular compartments and within different developmental and neuron type-specific contexts. Graphical abstract

DOI: https://doi.org/10.1016/j.celrep.2021.109713

Cell Reports

Article

# The RNA-binding protein Musashi controls axon compartment-specific synaptic connectivity through *ptp69D* mRNA poly(A)-tailing

## Graphical abstract

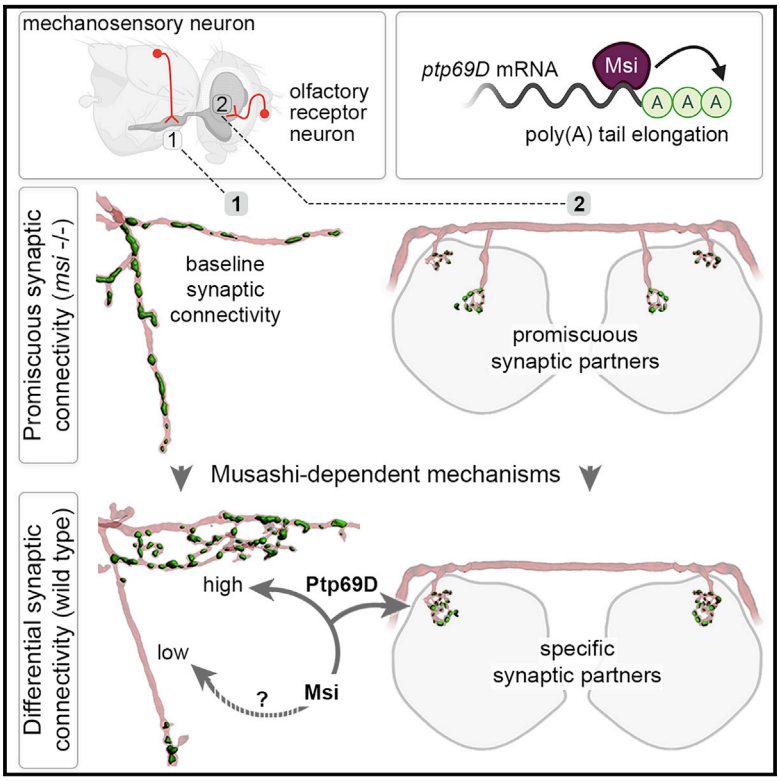


## Highlights

- Musashi controls axon branching and branch-specific synaptic connectivity in the CNS
- Musashi binds to the mRNA encoding the receptor protein tyrosine phosphatase Ptp69D
- Musashi and Ptp69D control wiring of both mechanosensory and olfactory sensory neurons
- Musashi promotes poly(A) tailing of the *ptp69D* mRNA and normal Ptp69D protein levels

## Authors

María Landínez-Macías, Weihong Qi, Anna Bratus-Neuenschwander, Martin Müller, Olivier Urwyler

## Correspondence

olivier.urwyler@uzh.ch

## In brief

Landínez-Macías et al. show that the RNA-binding protein Musashi differentially controls synaptic connectivity in distinct subcellular compartments of the same CNS axon, either promoting or repressing synapse allocation to specific compartments. Musashi post-transcriptionally stimulates the expression of the receptor protein tyrosine phosphatase Ptp69D, revealing a mechanism that shapes CNS circuit wiring.

Landínez-Macías et al., 2021, Cell Reports *36*, 109713
September 14, 2021 
https://doi.org/10.1016/j.celrep.2021.109713

CellPress

Cell Reports

CellPress
OPEN ACCESS

Article

# The RNA-binding protein Musashi controls axon compartment-specific synaptic connectivity through *ptp69D* mRNA poly(A)-tailing

María Landínez-Macías,[1,2] Weihong Qi,[3] Anna Bratus-Neuenschwander,[3] Martin Müller,[1,4] and Olivier Urwyler[1,4,5,*]
[1]Department of Molecular Life Sciences (DMLS), University of Zurich, Winterthurerstrasse 190, 8057 Zurich, Switzerland
[2]Molecular Life Sciences Program, Life Science Zurich Graduate School, University of Zurich, and ETH Zurich, 8057 Zurich, Switzerland
[3]Functional Genomics Center Zurich, ETH Zurich and University of Zurich, 8057 Zurich, Switzerland
[4]Neuroscience Center Zurich, University of Zurich and ETH Zurich, 8057 Zurich, Switzerland
[5]Lead contact
*Correspondence: olivier.urwyler@uzh.ch
https://doi.org/10.1016/j.celrep.2021.109713

## SUMMARY

Synaptic targeting with subcellular specificity is essential for neural circuit assembly. Developing neurons use mechanisms to curb promiscuous synaptic connections and to direct synapse formation to defined subcellular compartments. How this selectivity is achieved molecularly remains enigmatic. Here, we discover a link between mRNA poly(A)-tailing and axon collateral branch-specific synaptic connectivity within the CNS. We reveal that the RNA-binding protein Musashi binds to the mRNA encoding the receptor protein tyrosine phosphatase Ptp69D, thereby increasing poly(A) tail length and Ptp69D protein levels. This regulation specifically promotes synaptic connectivity in one axon collateral characterized by a high degree of arborization and strong synaptogenic potential. In a different compartment of the same axon, Musashi prevents ectopic synaptogenesis, revealing antagonistic, compartment-specific functions. Moreover, Musashi-dependent Ptp69D regulation controls synaptic connectivity in the olfactory circuit. Thus, Musashi differentially shapes synaptic connectivity at the level of individual subcellular compartments and within different developmental and neuron type-specific contexts.

## INTRODUCTION

The complexity of specifying synaptic connectivity in the developing central nervous system (CNS) is daunting. A large body of work has identified several mechanistic principles that address specificity but also flexibility for neural wiring (Dorskind and Kolodkin, 2021; Favuzzi et al., 2019; Hassan and Hiesinger, 2015; Linneweber et al., 2020; Riccomagno and Kolodkin, 2015; Sanes and Zipursky, 2020; Wang and Clandinin, 2016; Yogev and Shen, 2014). In particular, cell-surface receptors and adhesion molecules have been recognized as key mediators of neurite targeting (de Wit and Ghosh, 2016; Sperry, 1963). They play instructive roles in axon guidance and in the targeting of neuronal terminals to neuropil structures (Matsuoka et al., 2011; Timofeev et al., 2012; Xie et al., 2017; Yamagata and Sanes, 2008). Cell-surface proteins are also potent inducers of synapse formation *in vitro* (Biederer et al., 2002; Blockus et al., 2019; Scheiffele et al., 2000), but their role *in vivo* has not been clarified comprehensively (Sanes and Zipursky, 2020). The cell-type-specific temporal and quantitative transcriptional regulation of these factors is the subject of intense research efforts (Li et al., 2017; Földy et al., 2016). By contrast, the subsequent post-transcriptional control mechanisms remain less characterized in part due to significant technical challenges and a current lack of systematic approaches.

Post-transcriptional control of gene expression is prevalent in developing neurons (Loya et al., 2010). Alternative splicing of coding sequences (CDS) and untranslated regions (UTRs), mRNA transport, and local translation are crucially linked to correct axon guidance and branch formation (Feng et al., 2021; Shigeoka et al., 2016; Cagnetta et al., 2018, 2019; Jung et al., 2012; Koppers et al., 2019; Wong et al., 2017; Chen et al., 2008; Cioni et al., 2018; Holt et al., 2019). Moreover, during development, neuron-specific alternative polyadenylation endows transcripts with long 3′ UTRs, and this process affects neuronal connectivity (Hilgers et al., 2011; Miura et al., 2013; Zhang et al., 2019). *cis*-Regulatory elements in 3′ UTRs control mRNA stability, transport, localization, and (local) translation (Bae and Miura, 2020). They also have an impact on the regulation of mRNA poly(A) tail length, which is an important means to control mRNA stability and translation (Weill et al., 2012). However, in contrast to other post-transcriptional mechanisms, roles for poly(A) tail length regulation in neural circuit assembly and synaptic connectivity remain poorly understood.

Axon compartment-specific synapse number and location determine synaptic connectivity in specific CNS areas

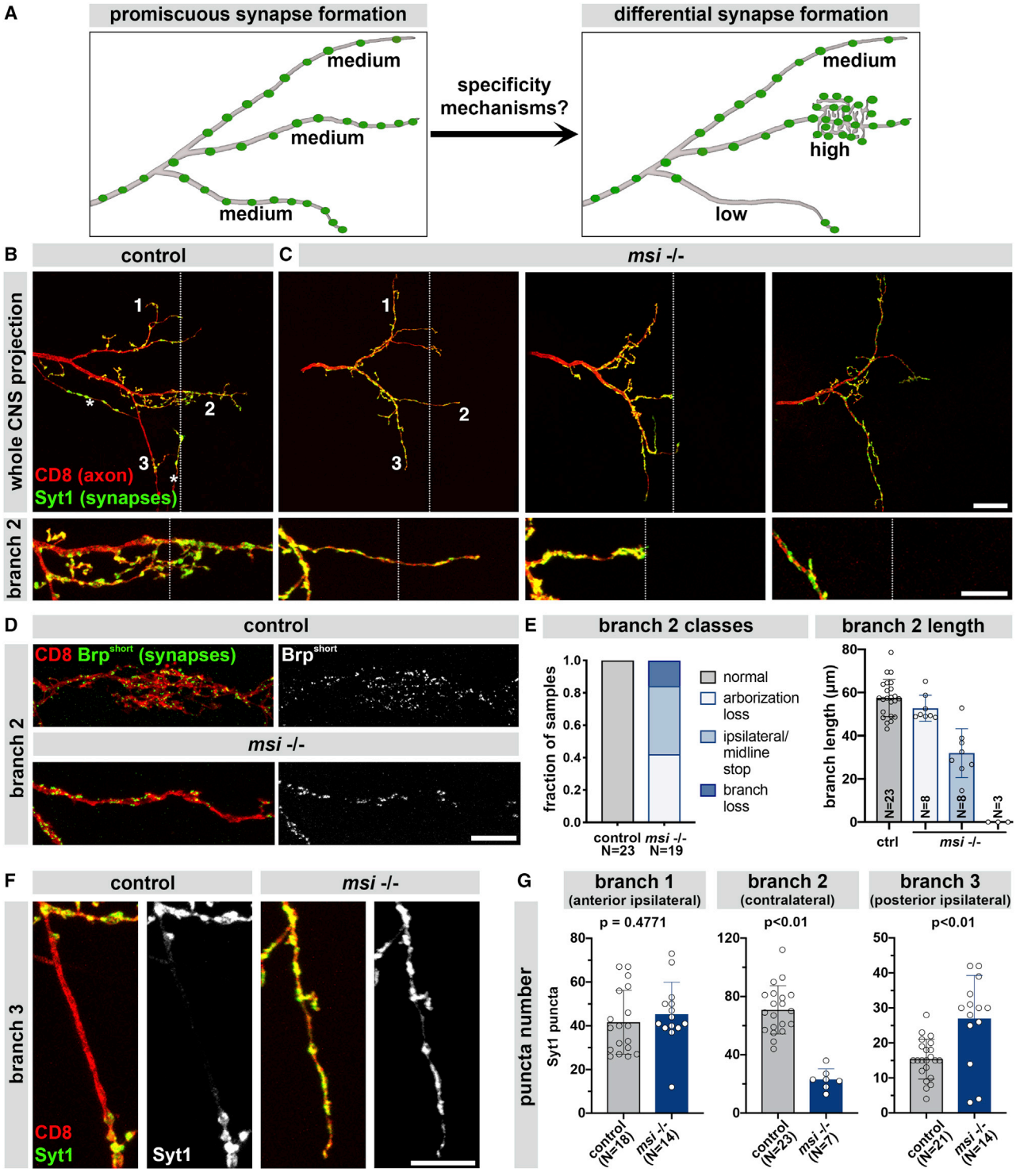


**Figure 1. Msi controls axon branching and branch-specific synaptic connectivity *in vivo* in the CNS**

(A) Schematics illustrating alternative models of synapse formation. Left, promiscuous synapse formation with similar density in all branches of a CNS axon ("medium" refers to synapse number). Right, molecular mechanisms determine the number and subcellular localization of presynapses specifically for each axon branch. The high number of synapses in the middle branch is enabled by terminal axon arborizations. In the bottom branch synapses are restricted subcellularly to the proximal-most and distal-most compartments.

(B) Axon projection of an MSN in a wild-type animal at the adult stage. CD8..GFP (pseudocolored in red) is a membrane marker, Cherry.Syt1 (green) is a marker for presynaptic vesicles. Numbers indicate the 3 stereotypic primary collateral branches, which, respectively, innervate ipsilateral anterior (1), contralateral (2), and

*(legend continued on next page)*

innervated by this axon. The need for axon compartment-specific control of synapse number becomes particularly evident when a single axon innervates disparate CNS target areas through the formation of collateral branches (Gibson and Ma, 2011; Hoersting and Schmucker, 2021; Kalil and Dent, 2014). Axons can form synapses promiscuously *in vitro*. How this promiscuity is curbed *in vivo* to ensure the proper subcellular/branch-specific location of synaptogenesis and correct synaptic partner choice remains elusive (Figure 1A). The determination of axon compartment-specific synaptic connectivity depends both on the formation of terminal arborizations and on synaptogenesis. As opposed to merely *en passant* synapses along the axon shaft, high synapse numbers at particular CNS locations are enabled by an increase in axon area through the formation of arborizations in which terminal synapses can form. Conversely, formation and stabilization of axon branches and arborizations depend on the recruitment of synaptic material, together with RNAs and mitochondria (Alsina et al., 2001; Constance et al., 2018; Courchet et al., 2013; Meyer and Smith, 2006; Ruthazer et al., 2006; Spillane et al., 2013; Wong et al., 2017), to the sites of branching and within immature axonal protrusions (“synaptotropic hypothesis”; Vaughn et al., 1974). Axon arbor architecture and synaptic connectivity are thus highly interdependent and controlled by common molecular mechanisms (Chia et al., 2014). Arbor formation and synaptogenesis together determine compartment-specific synaptic connectivity in axons.

Here, we assess pre-synapse number and location as a readout for compartment-specific synaptic connectivity. Using a genetic single-cell approach in the *Drosophila* CNS to study the RNA-binding protein Musashi (Msi) and the immunoglobulin (Ig)-superfamily receptor phosphatase Ptp69D, we discovered a link between the control of cell surface receptor expression through mRNA poly(A)-tailing and the spatial specificity of axon branching and synaptic connectivity. Msi has opposing functions in determining how two different subcellular compartments of the same sensory neuron connect with spatially separate CNS target cells. In one axon collateral Musashi increases terminal arbors and directly or indirectly the synapse number by controlling protein levels of Ptp69D through poly(A) tailing of its mRNA. By contrast, in a separate axon collateral, Msi restricts synapse formation via a currently unknown mechanism or different target. Our findings reveal the versatility of post-transcriptional mechanisms in specifying diverse and even opposing aspects of axon compartment-specific morphogenesis and synaptic connectivity.

## RESULTS

### Msi promotes axon branch formation and differentially controls axon compartment-specific synaptic connectivity

To study the mechanisms regulating CNS synaptic connectivity at the level of individual axons and axon collateral branches, we investigated *Drosophila* mechanosensory neurons (MSNs) that innervate large dorsocentral (DC) sensory bristles (Urwyler et al., 2015). Our genetic single-cell approach labels defined MSNs, ensuring analysis of the very same neuron in different animals (either the anterior DC or the posterior DC neuron). The number and distribution of presynapses were visualized with previously validated markers (Synaptotagmin 1 [Syt1] and Bruchpilot [Brp]; Fouquet et al., 2009; Zhang et al., 2002), which neither localize outside synapses nor induce additional synapses in MSNs (Urwyler et al., 2015). In the CNS, MSN axons form three invariable primary branches with specific and relatively stereotypic numbers and locations of presynapses (Figures 1B, S1B, and S1G; Urwyler et al., 2019).

A recent study on the role of the phosphatase Prl-1 suggested that post-transcriptional mechanisms may control axon branch-specific synaptogenesis in a cell-autonomous fashion (Urwyler et al., 2019). RNA-binding proteins (RBPs) are major post-transcriptional regulators of protein abundance, isoform diversification, localization/transport, and other functions (Glisovic et al., 2008). We therefore probed 11 candidate RBPs for cell-autonomous roles in synaptic connectivity, which was reduced in an axon compartment-specific way upon the knockdown of Msi (Figures S1C and S1D; see Table S1 for full genotypes throughout the article). We next used a null mutant (Nakamura et al., 1994) to assess the effects of complete loss of Msi. *msi*$^{-/-}$ animals displayed specific and robust defects in MSN synaptic connectivity (Figures 1 and S1). In all *msi* null mutant animals analyzed, the morphology of a specific axon collateral branch, the contralateral branch, was strongly affected, comprising phenotypes of the following three categories. First, in ~40% of cases, terminal synaptic arborizations are completely lost and presynapse number is profoundly decreased, while the primary axon branch still extended to the contralateral side of the CNS (Figures 1C, left panel, 1D, 1E, 1G, S1E, S1H, and S1J; Video S1). Second, in another ~40% of *msi* null animals, the primary axon branch fails to reach the contralateral side of the CNS and is arrested either on the ipsilateral side or at the midline

ipsilateral posterior (3) CNS target areas. The stochastic genetic approach labels either the anterior dorsocentral or the posterior dorsocentral MSN, which differ only in the length of branch 3. Dotted line represents the CNS midline. Asterisks indicate the processes of other, unrelated neurons, which were also labeled in this sample. The bottom panel shows a magnification of the contralateral branch.

(C) Different examples of whole-animal *msi* null mutant adult flies. Left, MSN with loss of contralateral branch synaptic arborizations; center, MSN whose contralateral branch extends only to the CNS midline; right, MSN completely lacking the contralateral branch.

(D) Reduced presynaptic active zone marker Bruchpilot$^{short}$ (Brp$^{short}$) in the contralateral branch of MSNs upon loss of Msi.

(E) Left, qualitative assessment of the contralateral branch phenotypes. The loss of *msi* leads to fully penetrant defects, with 3 phenotypic classes. Right, length of contralateral branches plotted for each phenotypic class.

(F) Loss of *msi* results in ectopic synapses in the posterior branch. Left, note the axon branch compartment devoid of Syt1 puncta in a wild-type animal. Right, in a *msi* null mutant, ectopic Syt1 puncta localize to that compartment.

(G) Numbers of Syt1 puncta for each primary branch/CNS target area, quantified from Imaris reconstructions (see Figure S1E).

Error bars represent standard deviations (SDs). Scale bars represent 20 μm in (C, top) and 10 μm in (C, bottom), (D), and (F). p values in (G) were calculated with unpaired t tests with Welch’s correction for branches 1 and 2, and with a Mann-Whitney test for branch 3.

See also Figure S1 and Videos S1 and S2.

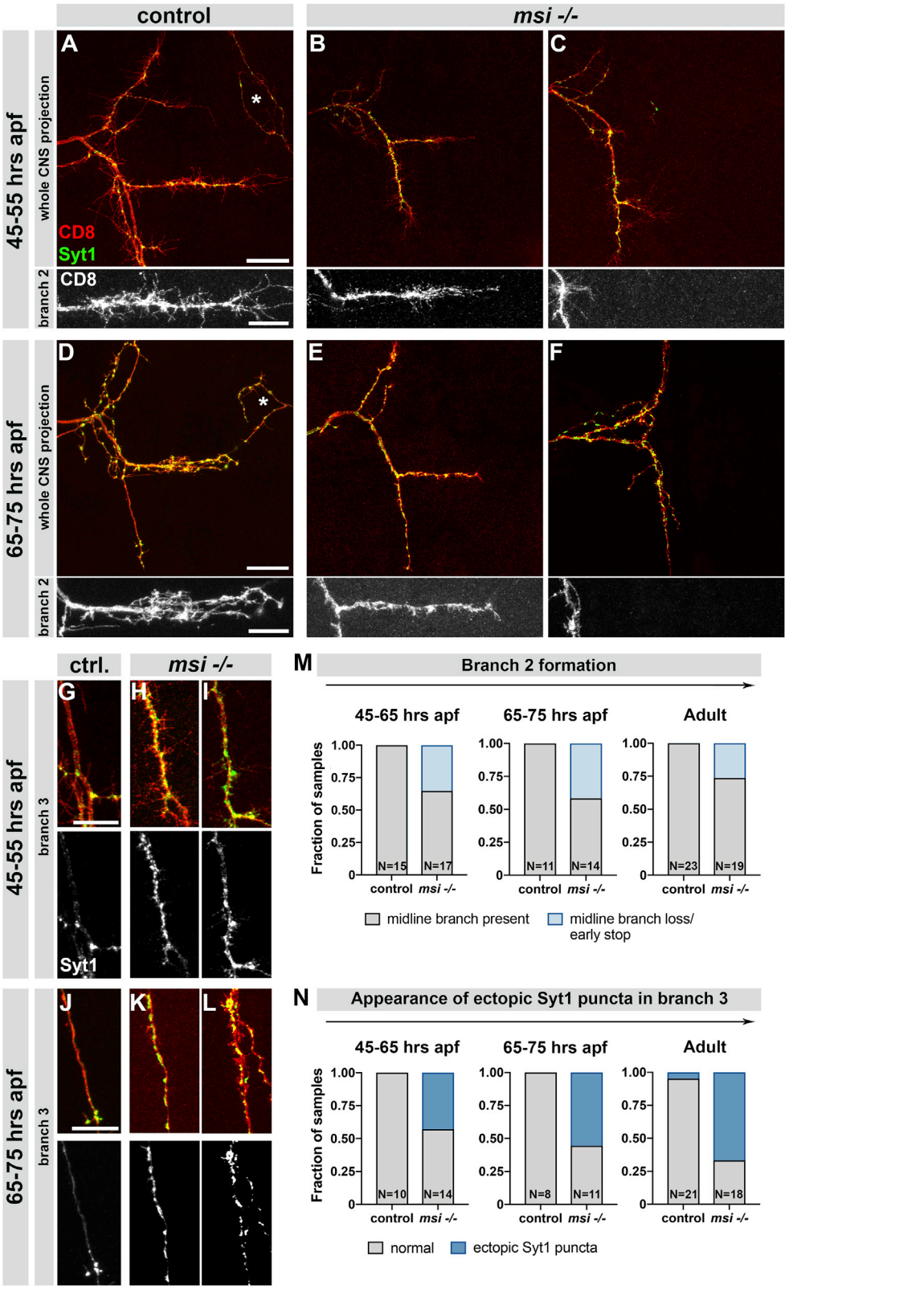


(legend on next page)

(Figures 1C, center panel, 1E, S1H, and S1J). Finally, in the remaining cases, the contralateral branch is completely missing (Figures 1C, right panel, 1E, S1H, and S1J). In animals lacking Msi, the density of presynapses on the primary branch was also significantly reduced in both full-length contralateral branches and branches of reduced length (Figure S1F, bottom panels). Thus, on the one hand Msi is required for contralateral primary branch formation and growth, and on the other hand, Msi also controls synapse density and synaptic arbor formation in this branch, resulting in a drastic reduction of synaptic connectivity upon the loss of Msi. Remarkably, in sharp contrast to the loss of synapses in the contralateral branch, we observed a robust increase in presynaptic marker puncta number in the posterior branch in roughly two-thirds of *msi*$^{-/-}$ animals (Figures 1F, 1G, S1E, S1F, and S1I). Moreover, these ectopic supernumerary synaptic marker puncta localized to a part of the posterior branch that is almost completely devoid of synapses in wild-type animals (Figures 1B, 1C, 1F, S1E, and S1I; Urwyler et al., 2015). By contrast, the anterior branch was unaffected by the loss of Msi (Figures 1C, 1G, S1E, and S1H). The branch-specific changes in synapse numbers in Msi mutants are unlikely due to a relocation or trafficking defect of the synaptic marker (see Discussion). Moreover, the cell fate specification of the analyzed MSNs appears to have occurred properly; as they correctly innervate their sensory bristle, they project their axon to the CNS, and elaborate and properly target the three stereotypic primary branches. Our results reveal that Msi selectively promotes synaptic connectivity in one axon branch, while opposing synaptic connectivity in another branch, suggesting axon compartment-specific control of synapse number by this RBP.

### Msi is required for branch and synapse patterning at early stages of axon targeting

To dissect the cellular morphogenesis events in which Msi is implicated during the wiring of MSNs, we performed a developmental analysis at different stages of axon targeting to the CNS (Figures 2 and S2). At approximately mid-pupal development (45–55 h after puparium formation, apf), the contralateral branch grows and projects across the CNS midline in control animals (Figure 2A; Urwyler et al., 2019). Synaptic material localizes to the branch, and filopodia-like protrusions sprout in regions where synaptic arborizations will form later (Figure 2A, lower panel; Urwyler et al., 2019). Approximately 20 h later (65–75 h apf), synaptic material is present in newly formed arborizations and satellite growth cones (Figure 2D; Dascenco et al., 2015; Urwyler et al., 2019). Protrusions originate from satellite growth cones at this stage to form the terminal network of synaptic arborizations. In animals lacking Msi, filopodial protrusions sprout when the primary branch projects toward the contralateral side at early targeting stages (45–55 h apf; Figures 2B and S2A). However, at the later stage (65–75 h apf), the contralateral branch almost entirely lacks both the satellite growth cones and the filopodial protrusions that sprout from them and precede the formation of terminal arborizations (Figures 2E, lower panel, S2A, and S2B). These data indicate that upon the loss of Msi, the contralateral branch grows timely, filopodial protrusions form normally, while satellite growth cones and terminal synaptic arborizations fail to form, rather than being pruned later. At both developmental stages analyzed, the contralateral branch was not present in ~40% of animals (Figures 2C, 2F, and 2M). This is comparable to or even higher than the percentage of adult animals, in which the contralateral branch is strongly shortened (Figure 2M). Thus, in the animals in which the primary branch has not extended properly, this defect appears to be due to impaired branch formation rather than branch retraction at a late time point.

In the posterior branch, presynaptic material is localized with remarkable spatial specificity already at early stages of branch development in control animals (Figure 2G). We observed precise marker localization to the distal tip of the posterior branch at 45–55 h apf, without signal in the axon compartment that also lacks synapses in adults in wild type (compare adult controls in Figure 1F with Figure 2G). We did not observe ectopic synaptic marker accumulation in any control sample at either of the two developmental stages analyzed (Figures 2G, 2J, 2N, and S2C). In sharp contrast, ectopic presynaptic material was observed at both stages in *msi* null mutant animals (Figures 2H, 2I, 2K, 2L, 2N, and S2C). The fraction of MSNs with ectopic synaptic marker localization was similar at both developmental stages and in adults (Figure 2N). In summary, our data show that upon the loss of Msi, axon branch and synapse defects

**Figure 2. Msi controls branch and synapse formation early during axon morphogenesis.**

(A–C, G–I) Animals in a time window from 45 to 55 h apf (corresponding to ~50% pupal development).

(A) MSN in a control animal extends numerous filopodial protrusions. Bottom panel, magnification of the developing contralateral branch (CD8, axon marker).

(B and C) Examples of *msi* loss of function animals, in which the contralateral branch is formed and not formed, respectively.

(D–F, J–L) Animals in a time window from 65 to 75 h apf.

(D) Wild-type animal, with satellite growth cones (secondary structures with filipodia at their tip) formed by the contralateral projection.

(E) *msi* loss of function animal. Satellite growth cones are absent in the contralateral branch (bottom panel).

(F) *msi* loss of function animal. The contralateral branch is absent.

(G and J) Magnifications of the posterior branch in the control animals shown in (A) and (D), respectively. Note the synapse-less region.

(H, I, K, and L) Magnifications of the posterior branches of mutant animals shown in (B), (C), (E), and (F), respectively. Note the ectopic localization of the Syt1 marker.

(M) Quantification of contralateral branch presence at 45–55 h apf, 65–75 h apf, and in adults, respectively, revealing no difference between the 3 stages (p value Pearson chi-square test = 0.7963, n = 50).

(N) Quantification of ectopic localization of presynaptic marker in the posterior branch at 45–55 h apf, 65–75 h apf, and at the adult stage, respectively, revealing no difference between the 3 stages (p value Pearson chi-square test = 0.404, n = 43).

Scale bars represent 20 μm in (A) and (D) (top) and 10 μm in (A), (D) (bottom), (G), and (J). Asterisks in (A) and (D) indicate the axonal processes of other, unrelated neurons.

See also Figure S2.

are present early, without major progressive changes during development. Msi therefore appears to play a role in branch and synapse formation, rather than in their stabilization/maintenance at later developmental stages.

### Msi and Ptp69D direct axon branch development and synaptic connectivity via the same genetic pathway

The loss of function of the receptor protein tyrosine phosphatase Ptp69D causes the loss of contralateral branch formation in MSNs innervating scutellar bristles (Dascenco et al., 2015). These MSNs lack the extensive contralateral branch synaptic arborizations observed in MSNs innervating the dorsocentral bristles, but otherwise have a very similar axon projection pattern in the CNS (Urwyler et al., 2019). We found that in dorsocentral MSNs, partial loss of *ptp69D* reproduces all contralateral branch phenotypes observed in *msi* null mutants (Figures 3A–3F and S3A–S3C): (1) branch loss as previously reported for scutellar MSNs (Dascenco et al., 2015; Figure S3A, left panel); (2) full extension of the contralateral branch, but complete loss of synaptic arborizations (Figures 3D and 3E); and (3) contralateral branch arrest at the midline/on the ipsilateral side (Figures 3F and S3A, right panel).

We assessed Ptp69D expression in developing MSN axons using a construct containing the mCherry-tagged *ptp69D* CDS flanked by UTRs, which correspond to the endogenous *ptp69D* 5′ and 3′ UTRs. UTRs in mRNAs typically contain *cis*-acting elements critical for recognition by RBPs and other post-transcriptional regulators. Ptp69D.mCherry expressed from this transgene localizes to the MSN axon at the earliest stages of CNS targeting (Figure 3G, top panels). The signal is observed both at the tips of growing branches (branch growth cones) and in a punctate pattern along the main axon and developing branches. At later stages (Figure 3G, bottom panels), the Ptp69D.mCherry signal is enriched in areas where synapses will be located in the adult MSN, particularly at sites where filopodial protrusions sprout from the developing contralateral branch, and in satellite growth cones (Figure 3G, arrowhead in bottom panel). By contrast, at the same developmental stage, we did not detect *ptp69D.mCherry* RNA in axons by fluorescent *in situ* hybridization (Figure S3H), suggesting that local translation may not be involved or that the mRNA is below the minimal detection levels for this method. Thus, Ptp69D protein is present at the time and place in which synaptogenesis occurs in MSNs, consistent with a model proposing that Ptp69D controls branch-specific synaptic connectivity.

We used loss-of-function mutants to test for genetic interactions between *ptp69D* and *msi* and to address whether the two gene products act in the same pathway. MSNs in animals that are heterozygous for either *ptp69D* or *msi* did not display any defects in synaptic connectivity (Figures 3H, 3I, and 3K). By contrast, loss of one copy of both *msi* and *ptp69D* reduced contralateral branch synaptic arborizations and synapse numbers (Figures 3J and 3K). Moreover, removing one gene copy of *ptp69D* dominantly enhanced the expressivity of contralateral branch phenotypes in *msi* null mutant animals (Figures 3L–3N, and S3D). This is consistent with a model in which loss of Msi leads to reduction (but not complete loss) of Ptp69D protein expression (see below and Figure 6E). Under these circumstances, removing one *ptp69D* gene copy further reduces Ptp69D levels and enhances the phenotype. To gain further evidence for this model, we used a weakly expressing *ptp69D* transgene (containing endogenous *ptp69D* UTRs) and tested whether it can rescue synaptic connectivity defects in *msi* null mutant animals. Raising *ptp69D* expression levels partially suppressed contralateral branch phenotypes caused by the loss of Msi (Figures S3E and S3F). While it remains possible that Msi and Ptp69D also operate in parallel molecular pathways, our results support a model that places Ptp69D downstream of Msi for directing selective axon branch formation and compartment-specific synaptic connectivity in MSNs.

### Msi and Ptp69D cell autonomously control odorant receptor neuron wiring

We next investigated whether Msi plays roles in axon and synapse development in other neurons. We did not detect any defects in synaptic morphology or function at the larval neuromuscular junction upon loss of Msi (Figures S4A and S4B). By contrast, adult *msi* null mutants displayed strong locomotor defects (Video S2), suggesting abnormal development and/or function of CNS circuits other than mechanosensory circuits. We therefore turned to the well-characterized first synapse in the *Drosophila* olfactory system. Depending on the specific odorant receptor (or) expressed by a given odorant receptor neuron (ORN), the ORN axon is guided to 1 of 50 glomeruli in the antennal lobe, the brain region where it establishes synapses with 1 specific type of projection neuron (Hong and Luo, 2014). Upon RNAi-mediated knockdown of Msi specifically in or10a-expressing ORNs, we observed axon mistargeting to the VA7m glomerulus that is normally not innervated by this class of ORNs (Figures 4A, 4C, 4M, 4N, and S4F; see Figures S4C and S4D for efficacy of the RNAi line). The presynaptic marker Brp also localizes to the mistargeted VA7m glomerulus, indicating ectopic synapse formation of mistargeted ORNs (Figures 4D and S4F). This suggests that these ORNs form synapses onto projection neurons that would normally not be their synaptic partners, because projection neurons pre-pattern the developing antennal lobe before the arrival of ORN axons (Jefferis et al., 2004). As the RNAi construct is expressed with a driver derived from enhancer regions of the *or* gene (Fishilevich and Vosshall, 2005), our results reveal a cell-autonomous role of Msi in ORN targeting. Moreover, knockdown of Msi by this driver is induced after cell fate specification. Combined with the fact that these or10a enhancer regions are active in adult animals (i.e., driving the fluorescent reporters for axons and synapses), this strongly indicates that the fate of these neurons was specified properly and that axon mistargeting is not due to potential alterations in cell fate upon Msi knockdown. Similar defects were found in whole-animal *msi* null mutants (Figure S4E) and in mosaics with *msi* null mutant ORNs in an otherwise heterozygous *msi* mutant background (Figures 4E and 4F). Interestingly, in rare cases, wild-type ORNs also form a few ectopic synapses in the VA7m glomerulus (Figure 4M, "mild" phenotype category). This suggests that there is a certain potential for connecting to postsynaptic cells at this location. A similar potential for ectopic synapse formation is found in the posterior branch of wild-type

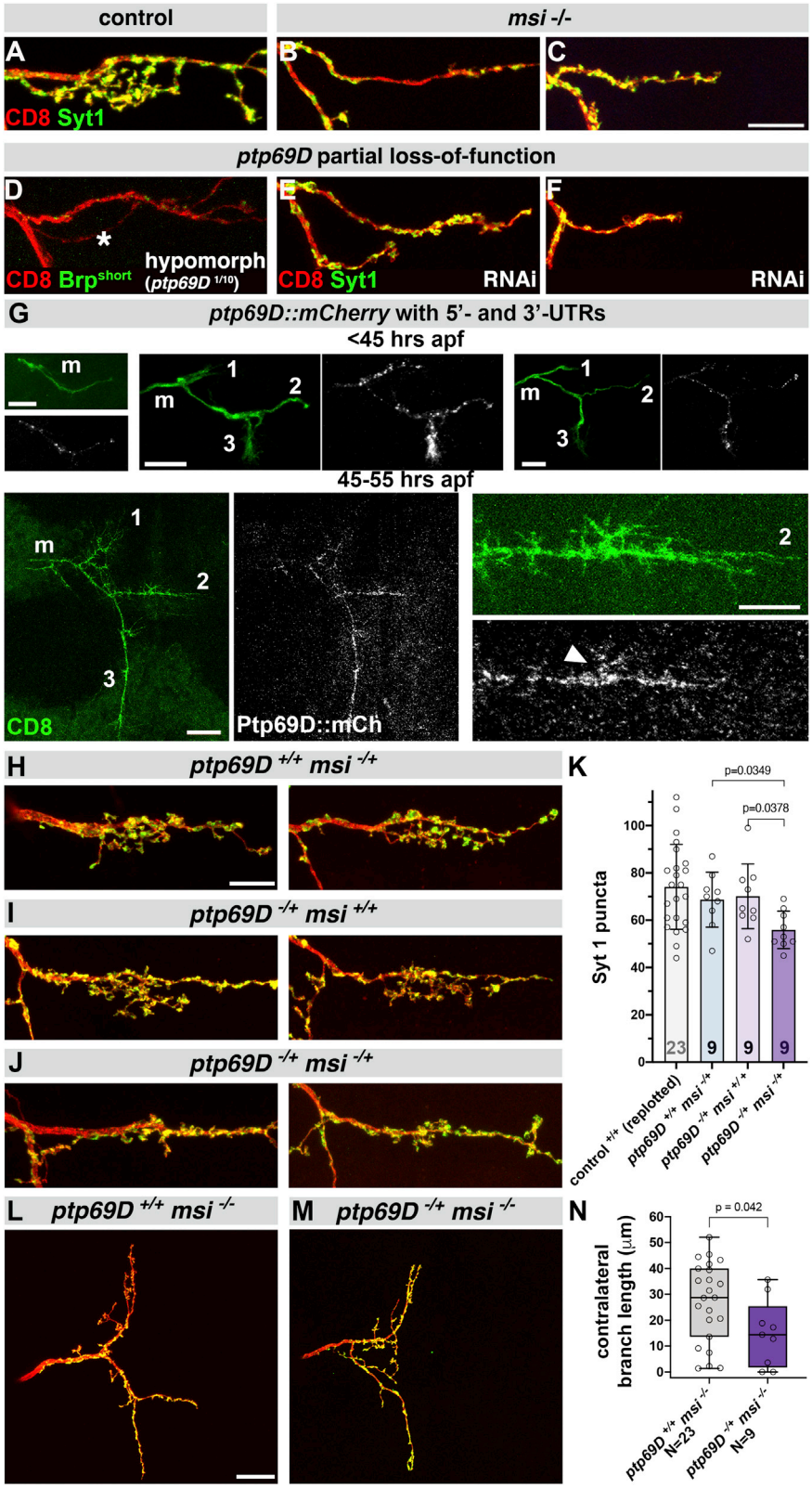


**Figure 3. Loss of *ptp69D* phenocopies loss of *msi*, and the 2 genes interact in MSNs**

(A) Contralateral branch of an MSN in a control animal.

(B and C) Contralateral branch of MSNs in *msi* null mutant animals. Scale bar represents 10 μm.

(D–F) Contralateral branch of MSNs in animals with a *ptp69D* hypomorphic allele combination (D) or with RNAi-mediated *ptp69D* knockdown in MSNs only (E and F). The asterisk in (D) indicates the axonal process of another, unrelated neuron.

(G) Cherry-tagged Ptp69D expressed in a single MSN during development, from a transgene with *ptp69D* UTR sequences. Top panels, 3 examples of expression before 45 h apf reveal a punctate localization in all 3 branches of MSNs, with enrichment in branch growth cones. m, main axon; 1, ipsilateral anterior; 2, contralateral; 3, ipsilateral posterior. Scale bars represent 10 μm. Bottom panels, expression between 45 and 55 h apf. Arrowhead points to a satellite growth cone with Ptp69D.Cherry signal. Scale bar represents 20 μm in the left panel and 10 μm in the magnified panel.

(H and I) Contralateral branch in *msi* and *ptp69D* heterozygous animals, respectively. Scale bar represents 10 μm.

(J) Contralateral branch in animals heterozygous mutant for both *msi* and *ptp69D*.

(K) Quantification of Syt1 puncta in the genotypes shown in (H)–(J). The values for the wild-type control are replotted from Figure 1. Error bars represent SDs; p values were calculated with a Kruskal-Wallis test.

(L and M) Full CNS projections of MSNs in a *msi* null mutant animal (L) and in an animal that is heterozygous for a *ptp69D* null mutation in combination with loss of *msi* (M), respectively. Scale bar represents 20 μm.

(N) Quantification of contralateral branch length in the genotypes shown in (L) and (M). Boxplots with median, 25%, and 75% percentiles are shown. p value was calculated with a Mann-Whitney test.

See also Figure S3 and Video S2.

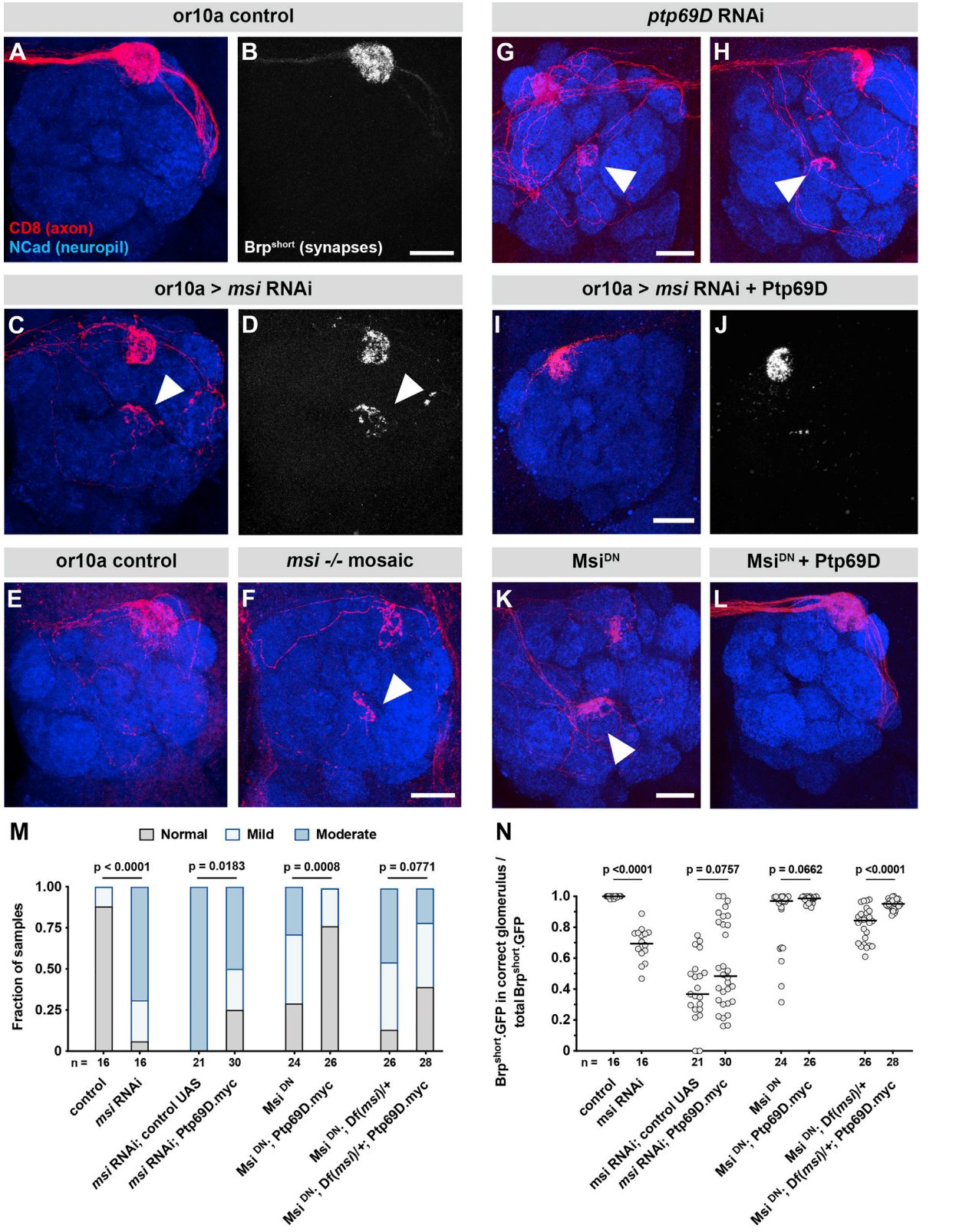


(legend on next page)

MSNs (Figures 1G and 2N), and in both cases, this potential is repressed by Msi-dependent mechanisms.

We next investigated *ptp69D* requirements and genetic interactions with *msi* in ORNs. In or10a-expressing ORNs, either RNAi-mediated knockdown of *ptp69D* or expression of a Msi construct that behaves as a dominant negative ($Msi^{DN}$; Video S2 and see next paragraph), induce axon mistargeting to the VA7m glomerulus, as does *msi* knockdown (Figures 4G, 4H, 4K, 4M, and 4N). Moreover, the expression of myc-tagged Ptp69D protein (Garrity et al., 1999) efficiently suppressed axon mistargeting and ectopic synapse formation induced by either Msi knockdown or $Msi^{DN}$ expression (Figures 4I–4N). These findings support the idea that Msi and Ptp69D also act in a common pathway for controlling ORN axon targeting. Our results reveal a cell-autonomous role for *msi* and *ptp69D* in the synaptic wiring of at least one ORN class.

## Msi binds to the *ptp69D* 3′ UTR

To determine whether the genetic interactions observed between Msi and Ptp69D are due to the direct binding of Msi to *ptp69D* mRNA, we performed a gene-specific "targets of RNA-binding proteins identified by editing" (TRIBE) approach (McMahon et al., 2016; Figure 5A). In short, the catalytic domain of the RNA-editing enzyme Adar ($Adar^{CD}$) was fused to the C terminus of full-length Msi ($Msi.Adar^{CD}$). When $Msi.Adar^{CD}$ binds to targets, the $Adar^{CD}$ catalyzes adenosine to inosine conversions in the target RNAs (which are read as guanosines in sequencing reactions). *In vivo*, $Msi.Adar^{CD}$ behaves as a dominant-negative protein (see above, labeled "$Msi^{DN}$" in previous paragraph). This could be caused by either steric hindrance of Msi interactions with other proteins or the editing events catalyzed by $Msi.Adar^{CD}$, which may affect the structure, stability, and/or translational efficiency of Msi RNA targets. Support for the latter is provided by our finding that increasing the editing efficiency of $Msi.Adar^{CD}$ by introducing a hyperactive mutation (referred to as "hyperTRIBE"; Rahman et al., 2018; Xu et al., 2018) led to lethality when the construct was expressed pan-neuronally.

$Msi.Adar^{CD}$ (without the hyperTRIBE mutation) and Ptp69D.mCherry (from a construct containing *ptp69D* UTR sequences) were co-expressed in all post-mitotic neurons, and total RNA was extracted from larval CNS. Editing events in the *ptp69D.mCherry* mRNA were identified by PacBio single-molecule sequencing (see Method details). Robust editing in the *ptp69D* 3′ UTR was observed in 2 biological replicates, with 32% (Figure S5A) and 5% (Figures 5B, center, and S5B) of the sequenced molecules with at least 1 A-to-I (G) transition, respectively. Discrepancies in total editing rates are likely due to biological variability and small differences in the rearing temperature of the flies and/or the developmental stage at which the CNS tissue was isolated. Remarkably, editing of the exact same adenosines was found in both replicates (Figures 5B, center, S5A, and S5B). In addition, in both samples, the same nucleotide positions showed the highest editing rates (A297 and A298). No editing events were observed without co-expression of $Msi.Adar^{CD}$, ruling out that *ptp69D* is a target of the endogenous ADAR enzyme. Furthermore, $Msi.Adar^{CD}$ did not edit a transgenically expressed negative control mRNA with a 3′ UTR of similar length (Figures 5B, top, and S5D), showing that $Msi.Adar^{CD}$ does not bind nonspecifically to any construct co-expressed in neurons. We neither observed substantial $Msi.Adar^{CD}$-driven editing events in the 5′ UTR or CDS of *ptp69D*, nor in 2 additional mRNAs, coding for Dscam1 and Elav, respectively (Figures S5E and S5F). This supports the specificity of $Msi.Adar^{CD}$ and its binding to genuine Msi targets.

To determine whether the 3′ UTR of *ptp69D* mRNA is sufficient for $Msi.Adar^{CD}$ binding, we used a construct containing the *ptp69D* 3′ UTR downstream of the CDS of Kaede fluorescent protein (*Kaede.ptp69D*$^{3'\ UTR}$). Co-expression of $Msi.Adar^{CD}$ and *Kaede.ptp69D*$^{3'\ UTR}$ produced editing events in 13% of the sequenced molecules (Figures 5B, bottom, and S5C). The editing events were found in the very same positions as in the experiments with *ptp69D.mCherry* described above. In summary, our results show that $Msi.Adar^{CD}$ selectively binds to the *ptp69D* 3′ UTR. Moreover, the reproducibility of the precise location of editing sites suggests that the binding specifically occurs to defined elements in the *ptp69D* 3′ UTR.

Next, we performed immunoprecipitation experiments coupled to quantitative reverse-transcription-PCR (qRT-PCR;

**Figure 4. *msi* and *ptp69D* are required cell autonomously and in the same genetic pathway for ORN wiring**

(A) Axons of ORNs that express the or10a odorant receptor target to the DL1 glomerulus in wild-type animals.

(B) Expression of $Brp^{short}$ presynaptic marker in or10a ORNs.

(C) RNAi-mediated *msi* knockdown leads to mistargeting of or10a ORNs to the VA7m glomerulus (arrowhead).

(D) $Brp^{short}$ signal is found in VA7m upon *msi* knockdown (arrowhead).

(E) Labeling of a subpopulation of or10a ORN axons with the MARCM technique in wild-type animals.

(F) *msi* null mutant MARCM clones in an otherwise mostly heterozygous animal; arrowhead indicates mistargeting to the VA7m glomerulus.

(G and H) RNAi-mediated knockdown of *ptp69D* leads to same mistargeting of or10a ORNs to the VA7m glomerulus (arrowheads).

(I and J) Expression of myc-tagged Ptp69D from a transgene without *ptp69D* UTRs in or10a ORNs suppresses the axon targeting (I) and ectopic synaptogenesis (J) defects caused by RNAi-mediated *msi* knockdown.

(K) Expression of $Msi.Adar^{CD}$ ($Msi^{DN}$) produces a dominant-negative phenotype, leading to mistargeting of or10a ORNs to VA7m (arrowhead).

(L) Expression of Ptp69D.myc (without *ptp69D* UTRs) suppresses the $Msi^{DN}$ phenotype.

(M) Quantification of or10a ORN axon targeting for the genotypes shown in (A)–(L), by an experimenter blinded to the genotypes. Mild: only very few axons mistarget to the VA7m glomerulus; Moderate: several axons innervate the VA7m glomerulus. The $Msi^{DN}$ phenotype is enhanced by deletion of 1 copy of endogenous *msi* ("Df(*msi*)"), which is also partially suppressed by expression of myc-tagged Ptp69D. p values were calculated with Pearson chi-square tests.

(N) Quantification of antennal lobe Brp signal for the genotypes shown in (A)–(L). The plot shows the ratio of $Brp^+$ pixels in the correct glomerulus (DL1) relative to the total amount of $Brp^+$ pixels in both DL1 and VA7m. p values were calculated with Mann-Whitney tests. See Method details. Scale bars represent 20 μm in all of the panels.

See also Figure S4.

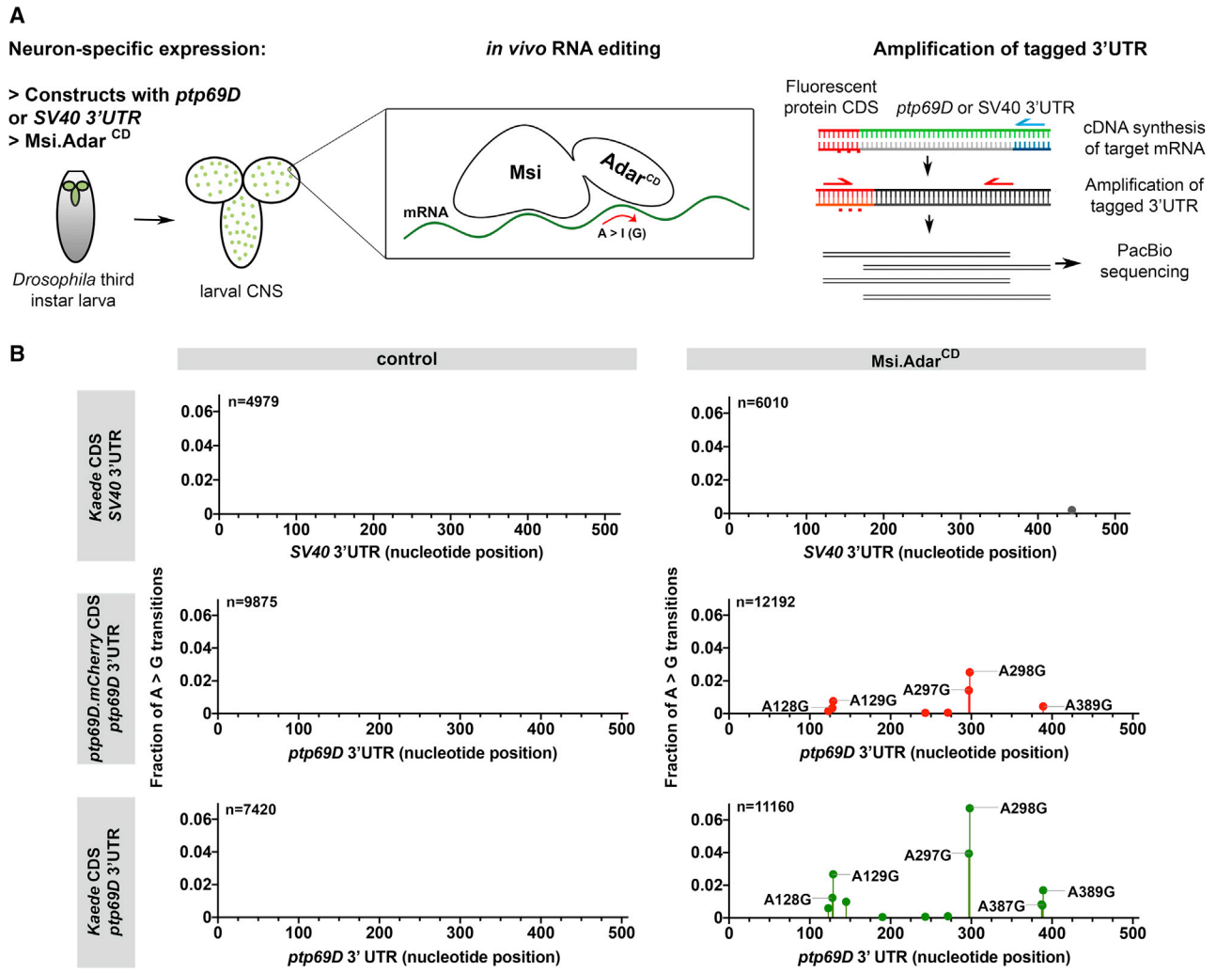


**Figure 5. A TRIBE approach reveals Msi binding to *ptp69D* mRNA**

(A) Strategy used for gene-specific TRIBE. Editing events are irreversible, allowing for the identification of all of the RNAs that had been bound by Msi.Adar$^{CD}$. Experimental mRNAs were co-expressed with Msi.Adar$^{CD}$ in neurons. RNA was extracted from third-instar larval CNS, and cDNA of the constructs of interest amplified as depicted in the panel at right.

(B) Top: negative control, SV40 3′ UTR located downstream of Kaede fluorescent protein coding sequence (CDS). In the 520-nt-long SV40 3′ UTR, only 1 editing site was observed, at a very low percentage (0.19%). Center: in a Cherry-tagged *ptp69D* construct (same as in Figure 3G), no editing events were observed in the absence of Msi.Adar$^{CD}$ in positions 1–508 of *ptp69D* 3′ UTR (corresponding to isoform 6, see Figure 6). Upon co-expression of Msi.Adar$^{CD}$, several editing events were found (see also Figure S5). Bottom: in a construct with Kaede CDS and *ptp69D* 3′ UTR (Kaede CDS *ptp69D* 3′ UTR), no editing events were observed in the absence of Msi.Adar$^{CD}$. With the co-expression of Msi.Adar$^{CD}$, editing events were found in the same positions as for the Cherry-tagged *ptp69D* construct (see also Figure S5). "n" indicates the total number of molecules sequenced.

See also Figure S5 and Video S2.

Figure S5G). In short, protein-RNA complexes were extracted from embryos or adult heads. Complexes of Msi bound to RNAs were precipitated with either an anti-Msi antibody or an anti-hemagglutinin (HA) antibody after pan-neuronal Msi.HA expression. Our qRT-PCR measurements revealed enrichment of both *ptp69D* mRNA and the positive control *tramtrack* mRNA (Bertolin et al., 2016) upon Msi immunoprecipitation (Figure S5G). By contrast, negative control mRNAs (*actin*, *tata-binding protein*) were not enriched. Thus, our immunoprecipitation (IP)/qRT-PCR results corroborate our TRIBE data, and the two orthogonal experimental approaches together provide strong evidence for the binding of the Msi protein to *ptp69D mRNA*.

Finally, we aimed at predicting Msi binding elements (MBEs) within the *ptp69D* 3′ UTR. The triplet UAG is critical in MBEs, and is often located within the larger sequence context of (G/A)$U_{1-3}$AGU pentamers-heptamers (Zearfoss et al., 2014). Depending on the 3′ UTR isoform (see below, Figure 6A and Table S2), up to 3 pentamers and 1 hexamer are present in the *ptp69D* 3′ UTR. MBEs preferentially occur in single-stranded RNA, with hairpin loops being the most favorable conformation (Uren et al., 2015). We predicted

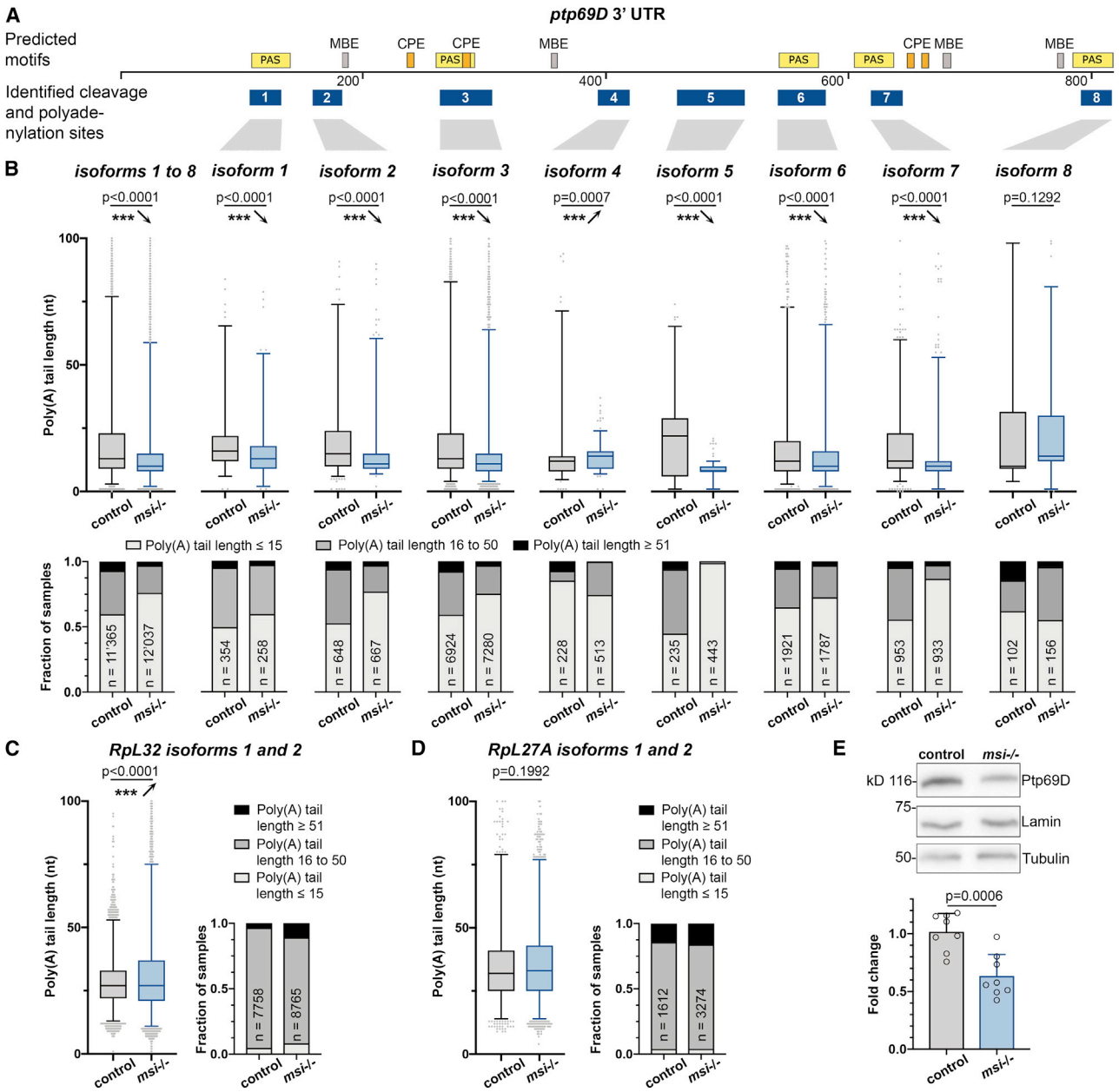


**Figure 6. Msi promotes polyadenylation of *ptp69D* mRNA to control Ptp69D protein levels in pupal heads**

(A) Schematic depicting alternative *ptp69D* 3′ UTR isoforms identified in a sPAT assay coupled to PacBio sequencing (see Method details). Blue boxes highlight the positions where cleavage and polyadenylation sites were identified. Eight alternative 3′ UTR isoforms were identified (see Table S2 for sequences). Cytoplasmic polyadenylation elements (CPEs, orange), and polyadenylation signals (PASs, yellow) were predicted with RegRNA 2.0 (Chang et al., 2013), and their locations are depicted on top. Msi binding elements (MBE, gray) with the sequence consensus (G/A)$U_{1-3}$AGU are also labeled.

(B) Poly(A) tail length in control and *msi* null mutant pupal heads at 48 h apf was measured by PacBio SMRT sequencing of molecules amplified by sPAT (see Method details). Results are shown for isoforms pooled together (leftmost plot, *isoforms 1 to 8*) and for individual 3′ UTR isoforms as in (A). Top plots: boxplots of poly(A) tail lengths, whiskers represent 2.5–97.5 percentiles. Outliers with values above 100 nt are not displayed. p values were calculated with Mann-Whitney tests. Downward arrows highlight poly(A) tail shortening in the *msi* null mutant; upward arrows highlight poly(A) tail extension. Bottom plots: fraction of samples with poly(A) tails in different size categories as indicated. "n" indicates total number of molecules sequenced.

(C) Slight enrichment of *RpL32* mRNA poly(A) tail lengths ≥51 nt in the *msi* mutant, while the median length is unchanged.

(D) Poly(A) tail length of *RpL27A* in the *msi* null mutant is not different from controls.

(E) Top, representative western blot for Ptp69D protein. Lamin and tubulin were used as loading controls. Extracts were prepared from pupal heads at 48 h apf. Bottom, densitometric quantification of Ptp69D protein levels, normalized to lamin. Error bars represent SDs of 8 technical replicates from 2 biological replicates. The p value was calculated with unpaired t test.

See also Figure S6 and Table S2.

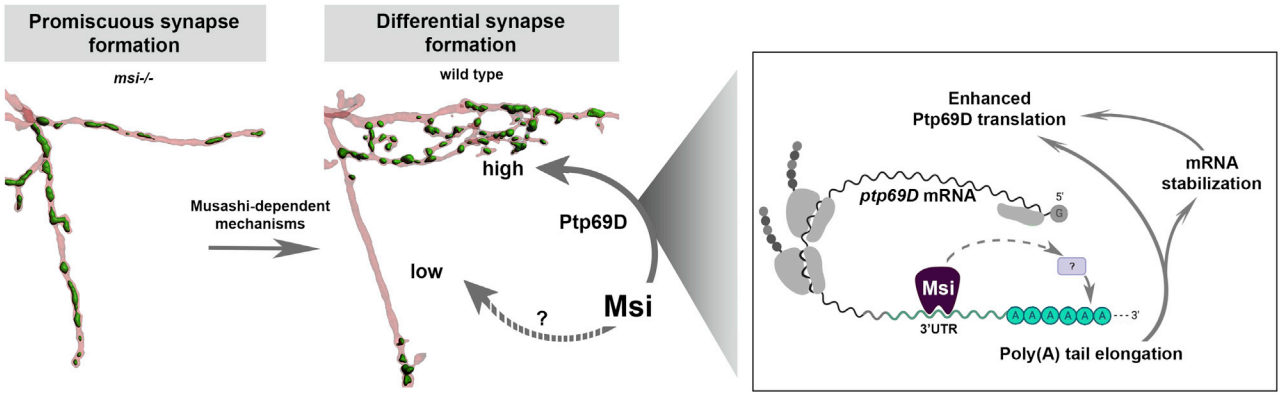


**Figure 7. Proposed model of Msi functions in branch-specific synapse formation**

(Left) promiscuous synapse formation in all axon collaterals (surface reconstructions of axon and synapses in a *msi* null mutant MSN). (Center) Msi-dependent mechanisms determine the number and subcellular localization of presynapses for the contralateral and posterior branches, respectively (reconstructions of axon and synapses in a wild-type animal). Msi and Ptp69D function cell autonomously in the contralateral branch. By contrast, restriction of the synapse location in the posterior branch by Msi, through an unknown target, may be cell autonomous or non-cell autonomous. (Right) molecular mechanism underlying the high synapse number in the contralateral branch. Msi binding to *ptp69D* mRNA enhances polyadenylation, stabilizes the mRNA, and stimulates its translation via different putative molecular mechanisms (see Discussion). Normal levels of *ptp69D* translation are required for the normal development of the contralateral branch.

with RNAfold (Gruber et al., 2008; Lorenz et al., 2011) the secondary structure of the *ptp69D* 3′ UTR isoform that we used for our TRIBE experiments (corresponding to isoform 6 below, see Figure 6A and Table S2), and looked for (G/A)$U_{1-3}$AGU in loops. Two potential canonical full-length MBEs are present in this *ptp69D* 3′ UTR: the pentamer GUAGU at position 184–188 in a double-stranded region and the pentamer AUAGU at position 356–360 in a hairpin loop (Figure S5H). It will be interesting in future studies to experimentally map whether Msi binds to the pentameric/hexameric MBEs, to the additional two trimeric (UAG), or the single tetrameric (AUAG) minimal consensus elements, or to other sequences that do not conform to a canonical MBE sequence (see Kuwako et al. [2010], for instance).

### Msi controls Ptp69D expression by increasing *ptp69D* mRNA poly(A) tail length

To determine the molecular function of Msi binding to the *ptp69D* 3′ UTR, we analyzed how the loss of Msi affects *ptp69D* mRNA and Ptp69D protein during development. We used a single-stranded DNA splint-mediated ligation assay (sPAT; Minasaki et al., 2014; see Method details) to identify putative alternative 3′ UTR isoforms of *ptp69D* mRNA. Eight alternative *ptp69D* 3′ UTRs that only differ in the selection of their polyadenylation signal (PAS), and thus in their 3′ end, were recovered from pupal head extracts of both control and *msi* mutant animals (48 h apf; Figure 6A; Table S2). The alternative *ptp69D* 3′ UTRs also differ in the number of putative MBEs (Figure 6A). In *msi* null mutants, levels of the 3 most abundant *ptp69D* 3′ UTR isoforms were slightly reduced; however, we did not observe changes in their relative distributions compared to wild-type animals (Figure S6B). This result suggests that Msi does not control *ptp69D* alternative polyadenylation site choice.

Msi can control the translation of mRNA targets via the regulation of poly(A) tail length (Cragle et al., 2019; Weill et al., 2017). In addition to being less efficiently translated, molecules with a very short poly(A) tail are unstable and subject to internal cleavage, 5′ decapping, and degradation (Couttet et al., 1997; Decker and Parker, 1993). Using a sPAT approach, we found that the poly(A) tail length of *ptp69D* mRNA is reduced in 6 of the 8 identified 3′ UTR isoforms in developing *msi* mutant animals (pupal head extracts at 48 h apf; Figures 6B, top, and S6D; see Legnini et al. [2019] for the PacBio sequencing of poly(A) tails). In particular, a larger fraction of clones with very short poly(A) tails ($\leq$15 nt) was found in the *msi* null mutant, while the number of clones with poly(A) tails longer than 50 nt was decreased (Figure 6B, bottom). These effects are especially pronounced in isoform 7 (Figure 6B), which is a highly abundant isoform (if not the most abundant isoform) in pupae at 48 h apf (Figure S6B). By contrast, the loss of *msi* did not decrease the poly(A) tail length of mRNAs coding for either RpL32 or Rpl27A, which were used as specificity controls (Figures 6C, 6D, and S6E). Consistent with roles for the poly(A) tail in translational regulation, Ptp69D protein levels were markedly reduced in developing *msi* null mutant animals (pupal heads and whole pupae, respectively, at 48 h apf; Figures 6E and S6G). These results show that Msi is critical for reaching normal Ptp69D protein levels and strongly suggest that Msi promotes *ptp69D* mRNA translation by increasing poly(A) tail length *in vivo* (Figure 7).

## DISCUSSION

### Control of axon compartment-specific synaptic connectivity in the CNS

Here, we study the poorly understood subcellular targeting of synaptic connectivity in CNS axons. We propose a model, in which all three primary MSN axon branches have a baseline potential to form synapses promiscuously, as observed for

vertebrate neurons grown *in vitro* (Figures 1A and 7; Scheiffele, 2003). In the posterior branch, Msi-dependent cell-autonomous or non-cell-autonomous mechanisms prevent synapse formation in a large domain of the branch, restricting synaptogenesis specifically to its most distal part (Figure 7). By contrast, in the contralateral branch, extensive terminal arborizations supporting a large number of synapses depend on cell-autonomous functions of Msi and Ptp69D (Figure 7). Synaptogenesis in the anterior branch does neither require Msi nor Ptp69D.

Targeting of synaptogenic signaling pathways to specific axon compartments by intracellular mechanisms such as local translation may contribute to the establishment of spatial specificity (Urwyler et al., 2019; Wong et al., 2017). In the case of Ptp69D, we did not find evidence for mRNA localization to axons and thus local translation. However, the previous finding that synaptogenic factors can be localized selectively to specific axon compartments (Urwyler et al., 2019) suggests that interactions with local cues could initiate compartmentalized specificity of Ptp69D function.

Our findings are consistent with the synaptotropic hypothesis (Constance et al., 2018; Özel et al., 2019; Ruthazer et al., 2006), in which the localization of synaptic material to specific axon locations is promoting the formation of filopodial protrusions and then their stabilization into terminal axon arborizations. These arborizations in turn are necessary to support a high number of synapses in this compartment. Remarkably, since refinement of axon compartment-specific filopodial protrusions correlates with glomerular targeting of ORNs (Kaur et al., 2019), the Msi-dependent targeting of ORNs could involve very similar cellular functions of Msi as in MSNs. Our data also reveal that Msi and Ptp69D are required repeatedly for the subsequent steps of axon branch development: first, the formation and growth of the primary axon branch (Dascenco et al., 2015 and this study), and second, the formation of synaptic arborizations and synapses. Such a repeated use of cell-surface receptors has, for example, also been found in ORN wiring (Joo et al., 2013; Li et al., 2018). Proper transcriptional and post-transcriptional control of the expression of cell-surface receptors is crucial to ensure their proper functioning in different steps of circuit wiring (Greer and Greenberg, 2008; Cagnetta et al., 2018; Petrovic and Hummel, 2008).

### Msi-dependent molecular mechanisms for axon compartment-specific synaptogenesis

One candidate pathway downstream of Msi/Ptp69D is through Dscam1 (Down syndrome cell adhesion molecule 1) signaling. Upon binding of the midline-secreted Slit extracellular ligand to Dscam1, Ptp69D directly dephosphorylates and inactivates Dscam1 (Dascenco et al., 2015). In the context of primary axon branch formation, this inactivation is required specifically in the contralateral branch of MSNs. Spatial specificity is thereby provided by the production of Slit at the CNS midline (Dascenco et al., 2015). Our results suggest an additional level of regulation, namely the tight control of Ptp69D levels by Msi. In the context of the formation of synaptic arbors and synapses that we uncover here, we speculate that an increased Dscam1 activity upon decreased Ptp69D levels leads to ectopic/excessive repulsion between the filopodia that sprout from the developing contralateral branch, or between synaptic partners (Hattori et al., 2008; He et al., 2014; Kise and Schmucker, 2013; Millard et al., 2010). This may prevent the formation of terminal synaptic arborizations and synapses.

Alternatively, the role of Ptp69D in the formation of synaptic arbors and synapses could be independent of Dscam1, given the well-established direct interactions of invertebrate and vertebrate type IIa Ptps with post-synaptic transmembrane proteins and with presynaptic organizers (Takahashi and Craig, 2013). However, the notion that these Ptps control CNS synaptogenesis has been challenged by the recent finding that the triple knockout of all type IIA Ptps in mice does not cause synapse formation defects in hippocampal neurons (Sclip and Südhof, 2020). Possibly reconciling these seemingly contradictory findings, our single-cell analysis reveals that Ptp69D is required for local synapse formation in a specific branch of a *Drosophila* CNS axon, rather than being generally required for synaptogenesis.

Depending on the cell type, Msi homologs may bind to >1,000 different RNAs (Uren et al., 2015; Weill et al., 2017). It could thus appear surprising that a single target (*ptp69D*) accounts for Msi function in MSN contralateral branch development. Interestingly, studies on alternative splicing in neurons have revealed highly cell-class-specific programs (Furlanis et al., 2019) and also identified remarkable specificity of only a few targets for a neuronal RBP (Traunmüller et al., 2016). Notably, our approach starting with the phenotypic analysis of a defined cell would favor the identification of a (few) select target(s). Nevertheless, Msi may have additional targets that are relevant for synaptogenesis in the MSN contralateral branch. An attractive candidate for such a target is the phosphatase Prl-1, which promotes synaptic arbor and synapse formation specifically in the MSN contralateral branch (Urwyler et al., 2019). However, in contrast to Msi and Ptp69D, Prl-1 does not have an additional function in the earlier step of contralateral primary branch formation and growth, providing further support for the notion that these are two distinct, separable developmental steps.

In the posterior branch of *Drosophila* MSNs, Msi-dependent mechanisms restrict synaptogenesis specifically to its most distal part and keep the synapse number low. Two observations suggest that the branch-specific changes in synapse numbers in *msi* mutants do not result from a simple relocation or trafficking defects of the synaptic marker. First, the increase in synaptic puncta in the posterior branch was much less pronounced than the loss of puncta in the contralateral branch (Figure 1G). Second, the loss of contralateral branch synapses occurs at full penetrance in *msi* null mutant animals, whereas ectopic synapses in the posterior branch are present only in approximately two-thirds of animals and do not correlate with the contralateral branch phenotypic class (Figure S1F). By contrast, Ptp69D does not appear to be required for restricting synaptogenesis in the posterior branch, although we cannot rule out that residual Ptp69D activity in the hypomorphic mutant combination and in the RNAi

situation masked such a function. We favor a model, in which at least one other, unknown Msi target functions to prevent ectopic synaptogenesis in the posterior branch. Therefore, we suggest that Msi controls the subcellular specificity of synaptic connectivity via divergent molecular targets, each reflected in axon branch-specific Msi functions (Figure 7). The identification of the Msi target that cell autonomously or non-cell autonomously restricts synapse formation to the distal end of the posterior branch is an important goal for future studies. Components of the plexin/semaphorin and Wnt signaling pathways are promising candidates due to their function in restricting presynapse formation in specific domains of *Caenorhabditis elegans* motoneuron axons (Mizumoto and Shen, 2013a; 2013b).

### Post-transcriptional regulation of Ptp69D by Msi

We show that Msi is promoting the polyadenylation of most *ptp69D* 3′ UTR isoforms, and propose that this counteracts mRNA degradation and keeps the *ptp69D* mRNA translationally active (Figure 7). In *Xenopus*, Msi activates the polyadenylation of targets at specific time points during the progression of meiosis (Arumugam et al., 2012; Charlesworth et al., 2006; Weill et al., 2017). A similar temporal regulation may be present during neuronal development to support the tight quantitative regulation of Ptp69D translation that is critical for correct neuronal wiring.

Previous reports suggest that Msi plays different roles in the control of polyadenylation and translation via several alternative or complementary molecular mechanisms. Binding of Msi to the 3′ UTR can elicit structural changes that preferentially expose some cytoplasmic polyadenylation elements (CPEs) (Weill et al., 2017). Alternatively, Msi can interact with the Gld2 poly(A) polymerase (Cragle and MacNicol, 2014). Finally, Msi can associate with poly(A) binding protein to promote the translation of mRNA targets (Cragle et al., 2019). Given that the molecular functions of Msi and Ptp proteins are highly conserved across species and broadly required for wiring of CNS circuits, the control of mRNA poly(A) tail length is poised to be a general mechanism underlying the subcellular specificity of synaptic connectivity in axons.

### Msi-dependent post-transcriptional mechanisms in different cellular contexts

Surprisingly, the roles of Msi in post-mitotic neurons remained largely elusive, with two notable exceptions. First, Msi controls synapse size and forgetting in *C. elegans* (Hadziselimovic et al., 2014). Second, Msi post-transcriptionally enhances Robo3 receptor expression in murine pre-cerebellar cells, to guide either the whole cells or their axons across the CNS midline (Kuwako et al., 2010). Remarkably, the mechanisms of regulation are fundamentally different for Robo3 and Ptp69D regulation, including binding of Msi to CDS versus 3′ UTR, and direct stimulation of translation versus enhancing poly(A) tailing. Thus, different receptors, which are crucial for different steps of circuit wiring, are distinctly regulated by Msi at the post-transcriptional level. The wide range of cellular and molecular functions of Msi thereby appear to depend not only on the cellular but also on the subcellular context. Further studies on Msi functions in the regulation of local synaptic connectivity will extend our understanding of how the architecture of neural circuits is established.

## STAR★METHODS

Detailed methods are provided in the online version of this paper and include the following:

- KEY RESOURCES TABLE
- RESOURCE AVAILABILITY
  - Lead contact
  - Materials availability
  - Data and code availability
- EXPERIMENTAL MODEL AND SUBJECT DETAILS
  - Fly stocks and genotypes
- METHOD DETAILS
  - Cloning of constructs
  - Immunostainings
  - Electrophysiology
  - RNA fluorescence *in situ* hybridization (RNA-FISH)
  - Sample preparation for TRIBE
  - Real-time PCR
  - Protein-RNA co-immunoprecipitation
  - Single-stranded DNA splint-mediated ligation assay to quantify poly(A) tails
  - Western blotting
  - Prediction of 3′ UTR folding
- QUANTIFICATION AND STATISTICAL ANALYSIS
  - Quantification of Synaptotagmin1 puncta
  - Phenotype quantification
  - RNA editing analysis for TRIBE
  - Real-time PCR
  - Quantification of poly(A) tail length
  - Western blot quantification

## SUPPLEMENTAL INFORMATION

Supplemental information can be found online at https://doi.org/10.1016/j.celrep.2021.109713.

## ACKNOWLEDGMENTS

We thank Dominika Grzejda and Valérie Hilgers (both at the Max Planck Institute of Immunobiology and Epigenetics, Freiburg, Germany); Alessia Soldano (University of Trento, Italy); and Sonu Sahadevan, Manuela Pérez-Berlanga, and Magdalini Polymenidou (University of Zurich) for advice on the IP experiments. We thank Dietmar Schmucker (LIMES, University of Bonn, Germany and VIB/KU Leuven, Belgium), Joris de Wit (VIB/KU Leuven, Belgium), and Stephan Urwyler for very constructive feedback on the manuscript. We are grateful to Erich Brunner, Esther Stoeckli, Damian Brunner, Katharina Schmidt (all at the University of Zurich) and Brian McCabe (EPF Lausanne, Switzerland) for critical input into the project. We thank Björn Meyer (Institut Pasteur, Paris, France) and Juan Diaz Quiroz (Marine Biological Laboratory, Woods Hole, MA, USA) for advice on RNA structure prediction and comments on TRIBE experiments. We thank Eliane Escher, Martin Moser, and Michael Daube (University of Zurich) for technical help. We thank Johannes Bischof and Konrad Basler (University of Zurich), Gary Hime (University of Melbourne, Australia), and Hideyuki Okano (Keio University, Tokyo, Japan) for reagents. Stocks obtained from the Bloomington Drosophila Stock Center (NIH P40OD018537) were used in this study. Monoclonal antibodies were obtained from the

Developmental Studies Hybridoma Bank, created by the NICHD of the NIH and maintained at The University of Iowa, Department of Biology, Iowa City, IA. This work was supported by grants from the Swiss National Science Foundation (Ambizione PZ00P3_161448, to O.U.; Assistant Professorship PP00P3_181036, to M.M.), grants from the Promotor Stiftung and from the Julius Klaus Stiftung to O.U., and funding from the University of Zurich.

## AUTHOR CONTRIBUTIONS

M.L.-M. and O.U. designed the project and the experiments, performed the experiments, and analyzed and interpreted the data. A.B.-N. prepared the library and sequencing for the PacBio SMRT sequencing experiments. W.Q. performed the bioinformatics analysis of the PacBio SMRT sequencing experiments. M.L.-M. and O.U. wrote the manuscript, and all of the authors edited the manuscript and accepted the final version. M.M. and O.U. acquired the funding.

## DECLARATION OF INTERESTS

The authors declare no competing interests.

Received: August 5, 2020
Revised: August 24, 2020
Accepted: August 24, 2021
Published: September 14, 2021

## SUPPORTING CITATIONS

The following references appear in the Supplemental information: Desai et al. (1994); Desai et al. (1996); Desai and purdy, (2003); Jan and Jan (1982); Morrison and Halder (2010); Parks et al. (2004); Zirin et al. (2020).

## REFERENCES

Alsina, B., Vu, T., and Cohen-Cory, S. (2001). Visualizing synapse formation in arborizing optic axons in vivo: dynamics and modulation by BDNF. Nat. Neurosci. *4*, 1093–1101.

Arumugam, K., MacNicol, M.C., Wang, Y., Cragle, C.E., Tackett, A.J., Hardy, L.L., and MacNicol, A.M. (2012). Ringo/cyclin-dependent kinase and mitogen-activated protein kinase signaling pathways regulate the activity of the cell fate determinant Musashi to promote cell cycle re-entry in Xenopus oocytes. J. Biol. Chem. *287*, 10639–10649.

Bae, B., and Miura, P. (2020). Emerging Roles for 3′ UTRs in Neurons. Int. J. Mol. Sci. *21*, 3413.

Bellaousov, S., and Mathews, D.H. (2010). ProbKnot: fast prediction of RNA secondary structure including pseudoknots. RNA *16*, 1870–1880.

Bertolin, A.P., Katz, M.J., Yano, M., Pozzi, B., Acevedo, J.M., Blanco-Obregón, D., Gándara, L., Sorianello, E., Kanda, H., Okano, H., et al. (2016). Musashi mediates translational repression of the Drosophila hypoxia inducible factor. Nucleic Acids Res. *44*, 7555–7567.

Biederer, T., Sara, Y., Mozhayeva, M., Atasoy, D., Liu, X., Kavalali, E.T., and Südhof, T.C. (2002). SynCAM, a synaptic adhesion molecule that drives synapse assembly. Science *297*, 1525–1531.

Bischof, J., Björklund, M., Furger, E., Schertel, C., Taipale, J., and Basler, K. (2013). A versatile platform for creating a comprehensive UAS-ORFeome library in Drosophila. Development *140*, 2434–2442.

Bischof, J., Maeda, R.K., Hediger, M., Karch, F., and Basler, K. (2007). An optimized transgenesis system for Drosophila using germ-line-specific phiC31 integrases. Proc. Natl. Acad. Sci. USA *104*, 3312–3317.

Blockus, H., Rolotti, S.V., Szoboszlay, M., Ming, T., Schroeder, A., Vennekens, K.M., Katsamba, P., Bahna, F., Mannepalli, S., Ahlsen, G., et al. (2019). Synaptogenic activity of the axon guidance molecule Robo2 is critical for hippocampal circuit function. bioRxiv. https://doi.org/10.1101/840710.

Cagnetta, R., Frese, C.K., Shigeoka, T., Krijgsveld, J., and Holt, C.E. (2018). Rapid Cue-Specific Remodeling of the Nascent Axonal Proteome. Neuron *99*, 29–46.e4.

Cagnetta, R., Wong, H.H.-W., Frese, C.K., Mallucci, G.R., Krijgsveld, J., and Holt, C.E. (2019). Noncanonical Modulation of the eIF2 Pathway Controls an Increase in Local Translation during Neural Wiring. Mol. Cell *73*, 474–489.e5.

Carrasco, J., Rauer, M., Hummel, B., Grzejda, D., Alfonso-Gonzalez, C., Lee, Y., Wang, Q., Puchalska, M., Mittler, G., and Hilgers, V. (2020). ELAV and FNE Determine Neuronal Transcript Signatures through EXon-Activated Rescue. Mol. Cell *80*, 156–163.e6.

Chang, T.-H., Huang, H.-Y., Hsu, J.B.-K., Weng, S.-L., Horng, J.-T., and Huang, H.-D. (2013). An enhanced computational platform for investigating the roles of regulatory RNA and for identifying functional RNA motifs. BMC Bioinformatics *14*, 1–8.

Charlesworth, A., Wilczynska, A., Thampi, P., Cox, L.L., and MacNicol, A.M. (2006). Musashi regulates the temporal order of mRNA translation during Xenopus oocyte maturation. EMBO J. *25*, 2792–2801.

Chen, Z., Gore, B.B., Long, H., Ma, L., and Tessier-Lavigne, M. (2008). Alternative splicing of the Robo3 axon guidance receptor governs the midline switch from attraction to repulsion. Neuron *58*, 325–332.

Chia, P.H., Chen, B., Li, P., Rosen, M.K., and Shen, K. (2014). Local F-actin network links synapse formation and axon branching. Cell *156*, 208–220.

Choi, H.M.T., Schwarzkopf, M., Fornace, M.E., Acharya, A., Artavanis, G., Stegmaier, J., Cunha, A., and Pierce, N.A. (2018). Third-generation *in situ* hybridization chain reaction: multiplexed, quantitative, sensitive, versatile, robust. Development *145*, dev165753.

Cioni, J.-M., Koppers, M., and Holt, C.E. (2018). Molecular control of local translation in axon development and maintenance. Curr. Opin. Neurobiol. *51*, 86–94.

Constance, W.D., Mukherjee, A., Fisher, Y.E., Pop, S., Blanc, E., Toyama, Y., and Williams, D.W. (2018). Neurexin and Neuroligin-based adhesion complexes drive axonal arborisation growth independent of synaptic activity. eLife *7*, e31659.

Courchet, J., Lewis, T.L., Jr., Lee, S., Courchet, V., Liou, D.-Y., Aizawa, S., and Polleux, F. (2013). Terminal axon branching is regulated by the LKB1-NUAK1 kinase pathway via presynaptic mitochondrial capture. Cell *153*, 1510–1525.

Couttet, P., Fromont-Racine, M., Steel, D., Pictet, R., and Grange, T. (1997). Messenger RNA deadenylylation precedes decapping in mammalian cells. Proc. Natl. Acad. Sci. USA *94*, 5628–5633.

Cragle, C., and MacNicol, A.M. (2014). Musashi protein-directed translational activation of target mRNAs is mediated by the poly(A) polymerase, germ line development defective-2. J. Biol. Chem. *289*, 14239–14251.

Cragle, C.E., Macnicol, M.C., Byrum, S.D., Hardy, L.L., Mackintosh, S.G., Richardson, W.A., Gray, N.K., Childs, G.V., Tackett, A.J., and MacNicol, A.M. (2019). Musashi interaction with poly(A) binding protein is required for activation of target mRNA translation. J. Biol. Chem. *28*, 10969–10986.

Dascenco, D., Erfurth, M.-L., Izadifar, A., Song, M., Sachse, S., Bortnick, R., Urwyler, O., Petrovic, M., Ayaz, D., He, H., et al. (2015). Slit and Receptor Tyrosine Phosphatase 69D Confer Spatial Specificity to Axon Branching via Dscam1. Cell *162*, 1140–1154.

de Wit, J., and Ghosh, A. (2016). Specification of synaptic connectivity by cell surface interactions. Nat. Rev. Neurosci. *17*, 22–35.

Decker, C.J., and Parker, R. (1993). A turnover pathway for both stable and unstable mRNAs in yeast: evidence for a requirement for deadenylation. Genes Dev. *7*, 1632–1643.

Desai, C., and Purdy, J. (2003). The neural receptor protein tyrosine phosphatase DPTP69D is required during periods of axon outgrowth in Drosophila. Genetics *164*, 575–588.

Desai, C.J., Popova, E., and Zinn, K. (1994). A Drosophila receptor tyrosine phosphatase expressed in the embryonic CNS and larval optic lobes is a member of the set of proteins bearing the "HRP" carbohydrate epitope. J. Neurosci. *14*, 7272–7283.

Desai, C.J., Gindhart, J.G., Jr., Goldstein, L.S., and Zinn, K. (1996). Receptor tyrosine phosphatases are required for motor axon guidance in the Drosophila embryo. Cell *84*, 599–609.

Dorskind, J.M., and Kolodkin, A.L. (2021). Revisiting and refining roles of neural guidance cues in circuit assembly. Curr. Opin. Neurobiol. *66*, 10–21.

Favuzzi, E., Deogracias, R., Marques-Smith, A., Maeso, P., Jezequel, J., Exposito-Alonso, D., Balia, M., Kroon, T., Hinojosa, A.J.F., Maraver, E., and Rico, B. (2019). Distinct molecular programs regulate synapse specificity in cortical inhibitory circuits. Science *363*, 413–417.

Feng, H., Moakley, D.F., Chen, S., McKenzie, M.G., Menon, V., and Zhang, C. (2021). Complexity and graded regulation of neuronal cell-type-specific alternative splicing revealed by single-cell RNA sequencing. Proc. Natl. Acad. Sci. USA *118*, e2013056118.

Fishilevich, E., and Vosshall, L.B. (2005). Genetic and functional subdivision of the Drosophila antennal lobe. Curr. Biol. *15*, 1548–1553.

Földy, C., Darmanis, S., Aoto, J., Malenka, R.C., Quake, S.R., and Südhof, T.C. (2016). Single-cell RNAseq reveals cell adhesion molecule profiles in electrophysiologically defined neurons. Proc. Natl. Acad. Sci. USA *113*, E5222–E5231.

Fouquet, W., Owald, D., Wichmann, C., Mertel, S., Depner, H., Dyba, M., Hallermann, S., Kittel, R.J., Eimer, S., and Sigrist, S.J. (2009). Maturation of active zone assembly by Drosophila Bruchpilot. J. Cell Biol. *186*, 129–145.

Furlanis, E., Traunmüller, L., Fucile, G., and Scheiffele, P. (2019). Landscape of ribosome-engaged transcript isoforms reveals extensive neuronal-cell-class-specific alternative splicing programs. Nat. Neurosci. *22*, 1709–1717.

Garrity, P.A., Lee, C.H., Salecker, I., Robertson, H.C., Desai, C.J., Zinn, K., and Zipursky, S.L. (1999). Retinal axon target selection in Drosophila is regulated by a receptor protein tyrosine phosphatase. Neuron *22*, 707–717.

Gibson, D.A., and Ma, L. (2011). Developmental regulation of axon branching in the vertebrate nervous system. Development *138*, 183–195.

Glisovic, T., Bachorik, J.L., Yong, J., and Dreyfuss, G. (2008). RNA-binding proteins and post-transcriptional gene regulation. FEBS Lett. *582*, 1977–1986.

Greer, P.L., and Greenberg, M.E. (2008). From synapse to nucleus: calcium-dependent gene transcription in the control of synapse development and function. Neuron *59*, 846–860.

Gruber, A.R., Lorenz, R., Bernhart, S.H., Neuböck, R., and Hofacker, I.L. (2008). The Vienna RNA websuite. Nucleic Acids Res. *36*, W70–W74.

Hadziselimovic, N., Vukojevic, V., Peter, F., Milnik, A., Fastenrath, M., Fenyves, B.G., Hieber, P., Demougin, P., Vogler, C., de Quervain, D.J.-F., et al. (2014). Forgetting is regulated via Musashi-mediated translational control of the Arp2/3 complex. Cell *156*, 1153–1166.

Hassan, B.A., and Hiesinger, P.R. (2015). Beyond Molecular Codes: Simple Rules to Wire Complex Brains. Cell *163*, 285–291.

Hattori, D., Millard, S.S., Wojtowicz, W.M., and Zipursky, S.L. (2008). Dscam-mediated cell recognition regulates neural circuit formation. Annu. Rev. Cell Dev. Biol. *24*, 597–620.

He, H., Kise, Y., Izadifar, A., Urwyler, O., Ayaz, D., Parthasarthy, A., Yan, B., Erfurth, M.-L., Dascenco, D., and Schmucker, D. (2014). Cell-intrinsic requirement of Dscam1 isoform diversity for axon collateral formation. Science *344*, 1182–1186.

Hilgers, V., Perry, M.W., Hendrix, D., Stark, A., Levine, M., and Haley, B. (2011). Neural-specific elongation of 3′ UTRs during Drosophila development. Proc. Natl. Acad. Sci. USA *108*, 15864–15869.

Hirota, Y., Okabe, M., Imai, T., Kurusu, M., Yamamoto, A., Miyao, S., Nakamura, M., Sawamoto, K., and Okano, H. (1999). Musashi and seven in absentia downregulate Tramtrack through distinct mechanisms in Drosophila eye development. Mech. Dev. *87*, 93–101.

Hoersting, A.-K., and Schmucker, D. (2021). Axonal branch patterning and neuronal shape diversity: roles in developmental circuit assembly: axonal branch patterning and neuronal shape diversity in developmental circuit assembly. Curr. Opin. Neurobiol. *66*, 158–165.

Holt, C.E., Martin, K.C., and Schuman, E.M. (2019). Local translation in neurons: visualization and function. Nat. Struct. Mol. Biol. *26*, 557–566.

Hong, W., and Luo, L. (2014). Genetic control of wiring specificity in the fly olfactory system. Genetics *196*, 17–29.

Jan, L.Y., and Jan, Y.N. (1982). Antibodies to horseradish peroxidase as specific neuronal markers in Drosophila and in grasshopper embryos. Proc. Natl. Acad. Sci. USA *79*, 2700–2704.

Jefferis, G.S.X.E., Vyas, R.M., Berdnik, D., Ramaekers, A., Stocker, R.F., Tanaka, N.K., Ito, K., and Luo, L. (2004). Developmental origin of wiring specificity in the olfactory system of Drosophila. Development *131*, 117–130.

Joo, W.J., Sweeney, L.B., Liang, L., and Luo, L. (2013). Linking cell fate, trajectory choice, and target selection: genetic analysis of Sema-2b in olfactory axon targeting. Neuron *78*, 673–686.

Jung, H., Yoon, B.C., and Holt, C.E. (2012). Axonal mRNA localization and local protein synthesis in nervous system assembly, maintenance and repair. Nat. Rev. Neurosci. *13*, 308–324.

Kalil, K., and Dent, E.W. (2014). Branch management: mechanisms of axon branching in the developing vertebrate CNS. Nat. Rev. Neurosci. *15*, 7–18.

Kaur, R., Surala, M., Hoger, S., Grössmann, N., Grimm, A., Timaeus, L., Kallina, W., and Hummel, T. (2019). Pioneer interneurons instruct bilaterality in the Drosophila olfactory sensory map. Sci. Adv. *5*, eaaw5537.

Kent, W.J. (2002). BLAT–the BLAST-like alignment tool. Genome Res. *12*, 656–664.

Kise, Y., and Schmucker, D. (2013). Role of self-avoidance in neuronal wiring. Curr. Opin. Neurobiol. *23*, 983–989.

Koppers, M., Cagnetta, R., Shigeoka, T., Wunderlich, L.C., Vallejo-Ramirez, P., Qiaojin Lin, J., Zhao, S., Jakobs, M.A., Dwivedy, A., Minett, M.S., et al. (2019). Receptor-specific interactome as a hub for rapid cue-induced selective translation in axons. eLife *8*, e48718.

Kuwako, K., Kakumoto, K., Imai, T., Igarashi, M., Hamakubo, T., Sakakibara, S., Tessier-Lavigne, M., Okano, H.J., and Okano, H. (2010). Neural RNA-binding protein Musashi1 controls midline crossing of precerebellar neurons through posttranscriptional regulation of Robo3/Rig-1 expression. Neuron *67*, 407–421.

Legnini, I., Alles, J., Karaiskos, N., Ayoub, S., and Rajewsky, N. (2019). FLAM-seq: full-length mRNA sequencing reveals principles of poly(A) tail length control. Nat. Methods *16*, 879–886.

Li, H. (2018). Minimap2: pairwise alignment for nucleotide sequences. Bioinformatics *34*, 3094–3100.

Li, H., Handsaker, B., Wysoker, A., Fennell, T., Ruan, J., Homer, N., Marth, G., Abecasis, G., and Durbin, R.; 1000 Genome Project Data Processing Subgroup (2009). The Sequence Alignment/Map format and SAMtools. Bioinformatics *25*, 2078–2079.

Li, H., Horns, F., Wu, B., Xie, Q., Li, J., Li, T., Luginbuhl, D.J., Quake, S.R., and Luo, L. (2017). Classifying Drosophila Olfactory Projection Neuron Subtypes by Single-Cell RNA Sequencing. Cell *171*, 1206–1220.e22.

Li, J., Guajardo, R., Xu, C., Wu, B., Li, H., Li, T., Luginbuhl, D.J., Xie, X., and Luo, L. (2018). Stepwise wiring of the *Drosophila* olfactory map requires specific Plexin B levels. eLife *7*, e39088.

Linneweber, G.A., Andriatsilavo, M., Dutta, S.B., Bengochea, M., Hellbruegge, L., Liu, G., Ejsmont, R.K., Straw, A.D., Wernet, M., Hiesinger, P.R., and Hassan, B.A. (2020). A neurodevelopmental origin of behavioral individuality in the *Drosophila* visual system. Science *367*, 1112–1119.

Lorenz, R., Bernhart, S.H., Höner Zu Siederdissen, C., Tafer, H., Flamm, C., Stadler, P.F., and Hofacker, I.L. (2011). ViennaRNA Package 2.0. Algorithms Mol. Biol. *6*, 26.

Loya, C.M., Van Vactor, D., and Fulga, T.A. (2010). Understanding neuronal connectivity through the post-transcriptional toolkit. Genes Dev. *24*, 625–635.

Martin, M. (2011). Cutadapt removes adapter sequences from high-throughput sequencing reads. EMBnet. J. *17*, 10–12.

Matsuoka, R.L., Chivatakarn, O., Badea, T.C., Samuels, I.S., Cahill, H., Katayama, K., Kumar, S.R., Suto, F., Chédotal, A., Peachey, N.S., et al. (2011).

Class 5 transmembrane semaphorins control selective Mammalian retinal lamination and function. Neuron *71*, 460–473.

McMahon, A.C., Rahman, R., Jin, H., Shen, J.L., Fieldsend, A., Luo, W., and Rosbash, M. (2016). TRIBE: Hijacking an RNA-Editing Enzyme to Identify Cell-Specific Targets of RNA-Binding Proteins. Cell *165*, 742–753.

Meyer, M.P., and Smith, S.J. (2006). Evidence from in vivo imaging that synaptogenesis guides the growth and branching of axonal arbors by two distinct mechanisms. J. Neurosci. *26*, 3604–3614.

Millard, S.S., Lu, Z., Zipursky, S.L., and Meinertzhagen, I.A. (2010). Drosophila dscam proteins regulate postsynaptic specificity at multiple-contact synapses. Neuron *67*, 761–768.

Minasaki, R., Rudel, D., and Eckmann, C.R. (2014). Increased sensitivity and accuracy of a single-stranded DNA splint-mediated ligation assay (sPAT) reveals poly(A) tail length dynamics of developmentally regulated mRNAs. RNA Biol. *11*, 111–123.

Miura, P., Shenker, S., Andreu-Agullo, C., Westholm, J.O., and Lai, E.C. (2013). Widespread and extensive lengthening of 3′ UTRs in the mammalian brain. Genome Res. *23*, 812–825.

Mizumoto, K., and Shen, K. (2013a). Interaxonal interaction defines tiled presynaptic innervation in C. elegans. Neuron *77*, 655–666.

Mizumoto, K., and Shen, K. (2013b). Two Wnts instruct topographic synaptic innervation in C. elegans. Cell Rep. *5*, 389–396.

Morrison, C.M., and Halder, G. (2010). Characterization of a dorsal-eye Gal4 Line in Drosophila. Genesis *48*, 3–7.

Nakamura, M., Okano, H., Blendy, J.A., and Montell, C. (1994). Musashi, a neural RNA-binding protein required for Drosophila adult external sensory organ development. Neuron *13*, 67–81.

Özel, M.N., Kulkarni, A., Hasan, A., Brummer, J., Moldenhauer, M., Daumann, I.-M., Wolfenberg, H., Dercksen, V.J., Kiral, F.R., Weiser, M., et al. (2019). Serial Synapse Formation through Filopodial Competition for Synaptic Seeding Factors. Dev. Cell *50*, 447–461.e8.

Parks, A.L., Cook, K.R., Belvin, M., Dompe, N.A., Fawcett, R., Huppert, K., Tan, L.R., Winter, C.G., Bogart, K.P., Deal, J.E., et al. (2004). Systematic generation of high-resolution deletion coverage of the Drosophila melanogaster genome. Nat. Genet. *36*, 288–292.

Petrovic, M., and Hummel, T. (2008). Temporal identity in axonal target layer recognition. Nature *456*, 800–803.

Poernbacher, I., Baumgartner, R., Marada, S.K., Edwards, K., and Stocker, H. (2012). Drosophila Pez acts in Hippo signaling to restrict intestinal stem cell proliferation. Curr. Biol. *22*, 389–396.

R Development Core Team (2013). R: A language and environment for statistical computing (R Foundation for Statistical Computing).

Rahman, R., Xu, W., Jin, H., and Rosbash, M. (2018). Identification of RNA-binding protein targets with HyperTRIBE. Nat. Protoc. *13*, 1829–1849.

Reuter, J.S., and Mathews, D.H. (2010). RNAstructure: software for RNA secondary structure prediction and analysis. BMC Bioinformatics *11*, 129.

Riccomagno, M.M., and Kolodkin, A.L. (2015). Sculpting neural circuits by axon and dendrite pruning. Annu. Rev. Cell Dev. Biol. *31*, 779–805.

Ruthazer, E.S., Li, J., and Cline, H.T. (2006). Stabilization of axon branch dynamics by synaptic maturation. J. Neurosci. *26*, 3594–3603.

Sanes, J.R., and Zipursky, S.L. (2020). Synaptic Specificity, Recognition Molecules, and Assembly of Neural Circuits. Cell *181*, 536–556.

Scheiffele, P. (2003). Cell-cell signaling during synapse formation in the CNS. Annu. Rev. Neurosci. *26*, 485–508.

Scheiffele, P., Fan, J., Choih, J., Fetter, R., and Serafini, T. (2000). Neuroligin expressed in nonneuronal cells triggers presynaptic development in contacting axons. Cell *101*, 657–669.

Schindelin, J., Arganda-Carreras, I., Frise, E., Kaynig, V., Longair, M., Pietzsch, T., Preibisch, S., Rueden, C., Saalfeld, S., Schmid, B., et al. (2012). Fiji: an open-source platform for biological-image analysis. Nat. Methods *9*, 676–682.

Sclip, A., and Südhof, T.C. (2020). LAR receptor phospho-tyrosine phosphatases regulate NMDA-receptor responses. eLife *9*, 7517.

Shigeoka, T., Jung, H., Jung, J., Turner-Bridger, B., Ohk, J., Lin, J.Q., Amieux, P.S., and Holt, C.E. (2016). Dynamic Axonal Translation in Developing and Mature Visual Circuits. Cell *166*, 181–192.

Sperry, R.W. (1963). Chemoaffinity in the orderly growth of nerve fiber patterns and connections. Proc. Natl. Acad. Sci. USA *50*, 703–710.

Spillane, M., Ketschek, A., Merianda, T.T., Twiss, J.L., and Gallo, G. (2013). Mitochondria coordinate sites of axon branching through localized intra-axonal protein synthesis. Cell Rep. *5*, 1564–1575.

Takahashi, H., and Craig, A.M. (2013). Protein tyrosine phosphatases PTPδ, PTPσ, and LAR: presynaptic hubs for synapse organization. Trends Neurosci. *36*, 522–534.

Timofeev, K., Joly, W., Hadjieconomou, D., and Salecker, I. (2012). Localized netrins act as positional cues to control layer-specific targeting of photoreceptor axons in Drosophila. Neuron *75*, 80–93.

Toggweiler, J., Willecke, M., and Basler, K. (2016). The transcription factor Ets21C drives tumor growth by cooperating with AP-1. Sci. Rep. *6*, 34725.

Traunmüller, L., Gomez, A.M., Nguyen, T.-M., and Scheiffele, P. (2016). Control of neuronal synapse specification by a highly dedicated alternative splicing program. Science *352*, 982–986.

Uren, P.J., Vo, D.T., de Araujo, P.R., Pötschke, R., Burns, S.C., Bahrami-Samani, E., Qiao, M., de Sousa Abreu, R., Nakaya, H.I., Correa, B.R., et al. (2015). RNA-Binding Protein Musashi1 Is a Central Regulator of Adhesion Pathways in Glioblastoma. Mol. Cell. Biol. *35*, 2965–2978.

Urwyler, O., Izadifar, A., Dascenco, D., Petrovic, M., He, H., Ayaz, D., Kremer, A., Lippens, S., Baatsen, P., Guérin, C.J., and Schmucker, D. (2015). Investigating CNS synaptogenesis at single-synapse resolution by combining reverse genetics with correlative light and electron microscopy. Development *142*, 394–405.

Urwyler, O., Izadifar, A., Vandenbogaerde, S., Sachse, S., Misbaer, A., and Schmucker, D. (2019). Branch-restricted localization of phosphatase Prl-1 specifies axonal synaptogenesis domains. Science *364*, eaau9952.

Vaughn, J.E., Henrikson, C.K., and Grieshaber, J.A. (1974). A quantitative study of synapses on motor neuron dendritic growth cones in developing mouse spinal cord. J. Cell Biol. *60*, 664–672.

Wang, I.E., and Clandinin, T.R. (2016). The Influence of Wiring Economy on Nervous System Evolution. Curr. Biol. *26*, R1101–R1108.

Weill, L., Belloc, E., Bava, F.-A., and Méndez, R. (2012). Translational control by changes in poly(A) tail length: recycling mRNAs. Nat. Struct. Mol. Biol. *19*, 577–585.

Weill, L., Belloc, E., Castellazzi, C.L., and Méndez, R. (2017). Musashi 1 regulates the timing and extent of meiotic mRNA translational activation by promoting the use of specific CPEs. Nat. Struct. Mol. Biol. *24*, 672–681.

Wentzel, C., Delvendahl, I., Sydlik, S., Georgiev, O., and Müller, M. (2018). Dysbindin links presynaptic proteasome function to homeostatic recruitment of low release probability vesicles. Nat. Commun. *9*, 267.

Wilm, A., Aw, P.P.K., Bertrand, D., Yeo, G.H.T., Ong, S.H., Wong, C.H., Khor, C.C., Petric, R., Hibberd, M.L., and Nagarajan, N. (2012). LoFreq: a sequence-quality aware, ultra-sensitive variant caller for uncovering cell-population heterogeneity from high-throughput sequencing datasets. Nucleic Acids Res. *40*, 11189–11201.

Wong, A.C.-N., Luo, Y., Jing, X., Franzenburg, S., Bost, A., and Douglas, A.E. (2015). The Host as the Driver of the Microbiota in the Gut and External Environment of Drosophila melanogaster. Appl. Environ. Microbiol. *81*, 6232–6240.

Wong, H.H.-W., Lin, J.Q., Ströhl, F., Roque, C.G., Cioni, J.-M., Cagnetta, R., Turner-Bridger, B., Laine, R.F., Harris, W.A., Kaminski, C.F., and Holt, C.E. (2017). RNA Docking and Local Translation Regulate Site-Specific Axon Remodeling In Vivo. Neuron *95*, 852–868.e8.

Worpenberg, L., Paolantoni, C., Longhi, S., Mulorz, M.M., Lence, T., Wessels, H.-H., Dassi, E., Aiello, G., Sutandy, F.X.R., Scheibe, M., et al. (2021). Ythdf is a N6-methyladenosine reader that modulates Fmr1 target mRNA selection and restricts axonal growth in Drosophila. EMBO J. *40*, e104975.

Xie, X., Tabuchi, M., Brown, M.P., Mitchell, S.P., Wu, M.N., and Kolodkin, A.L. (2017). The laminar organization of the *Drosophila* ellipsoid body is

semaphorin-dependent and prevents the formation of ectopic synaptic connections. eLife *6*, e04577.

Xu, W., Rahman, R., and Rosbash, M. (2018). Mechanistic implications of enhanced editing by a HyperTRIBE RNA-binding protein. RNA *24*, 173–182.

Yamagata, M., and Sanes, J.R. (2008). Dscam and Sidekick proteins direct lamina-specific synaptic connections in vertebrate retina. Nature *451*, 465–469.

Yogev, S., and Shen, K. (2014). Cellular and molecular mechanisms of synaptic specificity. Annu. Rev. Cell Dev. Biol. *30*, 417–437.

Zearfoss, N.R., Deveau, L.M., Clingman, C.C., Schmidt, E., Johnson, E.S., Massi, F., and Ryder, S.P. (2014). A conserved three-nucleotide core motif defines Musashi RNA binding specificity. J. Biol. Chem. *289*, 35530–35541.

Zhang, Y.Q., Rodesch, C.K., and Broadie, K. (2002). Living synaptic vesicle marker: synaptotagmin-GFP. Genesis *34*, 142–145.

Zhang, Z., So, K., Peterson, R., Bauer, M., Ng, H., Zhang, Y., Kim, J.H., Kidd, T., and Miura, P. (2019). Elav-Mediated Exon Skipping and Alternative Polyadenylation of the Dscam1 Gene Are Required for Axon Outgrowth. Cell Rep. *27*, 3808–3817.e7.

Zirin, J., Hu, Y., Liu, L., Yang-Zhou, D., Colbeth, R., Yan, D., Ewen-Campen, B., Tao, R., Vogt, E., VanNest, S., et al. (2020). Large-Scale Transgenic *Drosophila* Resource Collections for Loss- and Gain-of-Function Studies. Genetics *214*, 755–767.

## STAR★METHODS

### KEY RESOURCES TABLE

| REAGENT or RESOURCE | SOURCE | IDENTIFIER |
|---|---|---|
| Antibodies | | |
| Mouse monoclonal anti-protein tyrosine phosphatase 69D | DSHB | 3F11; RRID: AB_528444 |
| Rat monoclonal anti cadherin, DN-(extracellular domain) | DSHB | DN-Ex #8; RRID: AB_528121 |
| Mouse monoclonal anti-Lamin | DSHB | ADL67.10; RRID: AB_528336 |
| Mouse monoclonal anti-actin | Abcam | ab3280; RRID: AB_303668 |
| Mouse monoclonal anti-Musashi | H. Okano Lab, Keio Univ. | N/A. |
| Mouse monoclonal anti-GFP | Abcam | #ab1218; RRID: AB_298911 |
| Rabbit polyclonal anti-DsRed | Clontech | #632496; RRID: AB_10013483 |
| Mouse monoclonal anti-beta Tubulin | DSHB | E7; RRID: AB_528499 |
| Mouse monoclonal anti-Robo1 | DSHB | 13C9; RRID: AB_2181861 |
| Mouse monoclonal anti-HA antibody | BioLegend | 901501; RRID: AB_2565006 |
| Rat IgG isotype control | Invitrogen | 02-9602; RRID: AB_2532969 |
| HRP-conjugated anti-mouse | Jackson Immuno Research | 715-035-150; RRID: 2340770 |
| HRP-conjugated anti-rat | Jackson Immuno Research | 712-035-153; RRID: AB_2340639 |
| Alexa Fluor® 488 goat anti-mouse IgG | Invitrogen | A11029; RRID: AB_2534088 |
| Alexa Fluor ® 555 goat anti-rabbit IgG | Invitrogen | A21429; RRID: AB_2535850 |
| Alexa Fluor ® 633 goat anti-rabbit IgG | Invitrogen | A21094; RRID: AB_2535749 |
| Chemicals, peptides, and recombinant proteins | | |
| Paraformaldehyde | Merk | 8.18708.1000 |
| Triton X-100 | Sigma-Aldrich | X100 |
| SlowFadeTM Diamond Antifade Mountant | Invitrogen | S36972 |
| RNAlater™ | Sigma | R0901 |
| TRIzol® | Invitrogen | 15596-026 |
| Paraformaldehyde | Sigma-Aldrich | 158127 |
| Dulbecco's Phosphate Buffered Saline | Sigma-Aldrich | D8537 |
| Tween20 | Sigma-Aldrich | P9416 |
| Methanol | Carlo Erba | 414814 |
| Sodium chloride sodium citrate | Invitrogen | AM9770 |
| Critical commercial assays | | |
| DNA-*free*™ DNA removal kit | Invitrogen | AM1906 |
| Recombinant RNAsin® Ribonuclease Inhibitor | Promega | N2515 |
| GoScript reverse transcriptase | Promega | A5003 |
| Phusion® High-Fidelity DNA Polymerase | New England Biolabs | M0530 |
| AMPure XP | Beckman Coulter | A63880 |
| MESA Green qPCR™ Mastermix Plus for SYBR® assay | Eurogentec | RT-SY2X-03+WOU |
| cOmplete Mini protein inhibitor cocktail tablets | Roche | 11836170001 |
| Protein G Sepharose 4 Fast Flow beads | GE Healthcare | 17-0618-01 |
| T4 RNA ligase 2 | New England BioLabs | M0239S |
| Acrylamide | Bio-Rad Laboratories, Inc. | 161-0156 |
| Mini-PROTEAN TGX Stain-Free Gels | Bio-Rad Laboratories, Inc. | 4568033 |

(*Continued on next page*)

*Continued*

| REAGENT or RESOURCE | SOURCE | IDENTIFIER |
|---|---|---|
| Amersham Hybond P 0.45 PVDF | GE Healthcare Life science | 10600023 |
| Amersham ECL Western Blotting detection reagents | GE Healthcare Life science | RPN2232 |
| HCR v3.0 reagents for RNA-FISH | Molecular Instruments | N/A |
| SMRTbell Template Prep Kit 1.0 | Pacific Biosciences | 100-259-100 |
| SMRTbell Barcoded Adaptor Complete Prep-96 | Pacific Biosciences | 100-514-900 |
| SMRTbell Express Template Prep Kit 2.0 | Pacific Biosciences | 100-938-900 |
| Barcoded Overhang Adaptor Kit - 8A/8B | Pacific Biosciences | 101-628-400/500 |
| Sequel Binding and Internal Control Kit 3.0 | Pacific Biosciences | 101-626-600 |
| SMRT Cell 1M v3 | Pacific Biosciences | 101-531-000 |
| Sequel Sequencing Kits 3.0 | Pacific Biosciences | 101-597-900 |
| Experimental models: organisms/strains | | |
| See Table S1 for the list of the genotypes of *D. melanogaster* used in each figure. | N/A (See Table S1 for list of sources). | N/A |
| Oligonucleotides | | |
| See Table S3 for the list of primers for cloning, mutagenesis, TRIBE, real-time PCR, and single stranded DNA splint-mediated ligation assay | N/A (See Table S3 for list of sources). | N/A (See Table S3 for list of identifiers). |
| Recombinant DNA | | |
| Kaede-N1 plasmid | Addgene | RRID: Addgene_54726 |
| pUASattB | K. Basler lab, Univ. Zurich | Bischof et al., 2007 |
| pSC-A-amp/Kan | Agilent Technologies | 240205 |
| pJFRC-20X-UAS-ADARcd | Addgene | 81173 |
| pOt2 msi-RA | DGRC | LD31631 |
| pFlc-1-Ptp69D-RB | DGRC | RE06719 |
| Software and algorithms | | |
| Custom scripts for RNA editing (TRIBE) and poly(A) tail analyses | This paper | https://github.com/weihongqi/p3154; https://doi.org/10.5281/zenodo.5206822 |
| Fiji / ImageJ | https://fiji.sc | RRID: SCR_002285; https://doi.org/10.1038/nmeth.2019 |
| Prism 8 | GraphPad Software Inc. | RRID: SCR_002798; Version 8.0.2 |
| Imaris | Bitplane, an Oxford Instruments company | RRID: SCR_007370; version 9.5.1 |
| Igor Pro | WaveMetrics Inc. | RRID: SCR_000325; Version 6.37 |
| Clampex | Axon CNS, Molecular Devices | RRID: SCR_011323 |
| Adobe Photoshop | Adobe Systems Incorporated | RRID: SCR_014199 |
| RNAfold | Gruber et al., 2008; Lorenz et al., 2011 | RRID: SCR_008550 |
| SMRT Link | Pacific Biosciences | RRID: SCR_002942; version 7.0.1.66975 |
| minimap2 | Li, 2018 | RRID: SCR_018550; version 2.15r905 |
| lofreq | Wilm et al., 2012 | RRID: SCR_013054; version 2.1.2 |
| splitSNP | GitHub | https://github.com/astatham/splitSNP |
| samtools | Li et al., 2009 | RRID: SCR_002105; version 1.3.1 |
| seqtk | GitHub | RRID: SCR_018927; version 1.2-r102 |
| cutadapt | Martin, 2011 | RRID: SCR_011841; version 2.9 |
| blat | Kent, 2002 | RRID: SCR_011919; v. 36x1 |
| R | R Development Core Team, 2013 | RRID: SCR_001905 |

## RESOURCE AVAILABILITY

### Lead contact

Requests for resources and reagents should be directed to the Lead Contact, Olivier Urwyler (olivier.urwyler@uzh.ch). All reagents generated in this study are available from the Lead Contact.

### Materials availability

All the plasmids and *D. melanogaster* lines generated in this study are available from the Lead Contact without restriction.

### Data and code availability

All data reported in this paper will be shared by the lead contact upon request.

All original code has been deposited at Zenodo and is publicly available as of the date of publication. DOIs are listed in the Key resources table.

Any additional information required to reanalyze the data reported in this paper is available from the lead contact upon request.

## EXPERIMENTAL MODEL AND SUBJECT DETAILS

### Fly stocks and genotypes

*Drosophila melanogaster* specimens were maintained at 25°C with 12 hours day/night cycles. Genotypes for all figure panels are listed in Table S1. Sources of fly lines are also listed in Table S1. In all experiments, both females and males were used, and no differences were observed between sexes. Developmental stages are stated in the Figures/legends and/or in the Method details section.

## METHOD DETAILS

### Cloning of constructs

Construction of the Msi.Adar$^{CD}$ plasmid was done as follows. First, in the plasmid pOT2-*msi* (clone #LD31631 obtained from the *Drosophila* Genomics Resource Center, DGRC), a silent mutation was introduced into the *msi* coding sequence to disrupt the NotI site. This was done by site-directed mutagenesis with the primers 5′-CATGGAGAACGCGGCGGCAGCAGCCGCCGC and 5′-GCGGCGGCTGCTGCCGCCGCGTTCTCCATG (underlined nucleotide is the site of mutation in the NotI recognition sequence, changing the codon GCC to GCG, which both code for alanine). Then, the *msi* coding sequence was PCR-amplified from the mutated pOT2-*msi* plasmid with Phusion® High-Fidelity DNA Polymerase (New England Biolabs #M0530), using the primers 5′-ATAA GAATGCGGCCGCATGCACGCGCTTCAGGAAGG and 5′-ATAAGAATGCGGCCGCCCGACGTACATGCCCATGCCG to add NotI recognition sites to both ends (underlined). The PCR product was purified, digested with NotI, and ligated into NotI-digested pJFRC-20X-UAS-ADARcd (plasmid #81173 obtained from Addgene). One clone with the *msi* coding sequence inserted in the right orientation was selected, sequence-verified, and used for microinjection into embryos of genotype *yw P{nos-phiC31\int.NLS}$^{X}$;P{CaryP}$^{attP40}$* (performed at Rainbow Transgenic Flies, Inc., Camarillo, USA).

The construct coding for Cherry-tagged Ptp69D, including UTRs, was cloned as follows. First, in the plasmid pFlc-1-*ptp69D* (clone RE06719 obtained from the DGRC), an XhoI site (underlined below) was introduced at the 5′ end of the *ptp69D* 3′-UTR. This was done by site-directed mutagenesis using the primers 5′-CAACATTGGATTAACTCGAGTTAGATATGTATATAC and 5′-GTATATACATATC TAACTCGAGTTAATCCAATGTTG. Then, Cherry CDS was PCR amplified from the plasmid 20xUAS-FRT > STOP > FRT-mCD8::GFP-2A-mCherry::Syt1 (Urwyler et al., 2015) using the primers 5′-CCGCTCGAGATGGTGAGCAAGGGCGAG-3′ and 5′-CCGCTCGAGTTACTTGTACAGCTCGTCCATG-3′ (introducing XhoI sites at both ends) and GoTaq® G2 DNA Polymerase (Promega #M784B). This product was first TA-cloned using StrataClone PCR Cloning Kit (Agilent #240205) and subsequently digested with XhoI. The excised product was cloned into the XhoI site introduced into pFlc-1-*ptp69D*, and clones with the correct orientation were identified and sequence-verified by sequencing. The resulting plasmid was then mutagenized by site-directed mutagenesis with the primers 5′- GTCAACATTGGATGGATCCGGGATGGTGAGCAAG and 5′- CTTGCTCACCATCCCGGATCCATCCAATGTT-GAC to remove the stop codon at the end of the Cherry CDS and insert a Gly-Ser-Gly amino acid linker between Ptp69D and Cherry proteins. Then, the KpnI / NotI fragment of this plasmid, including *ptp69D* 5′-UTR and CDS, Cherry CDS, and *ptp69D* 3′-UTR, was subcloned into the KpnI / NotI sites of pUASattB (Bischof et al., 2007). Transgenic lines were created by microinjection of embryos of genotypes *y$^{1}$w$^{67}$c$^{23}$; P{CaryP}attP40*, at BestGene, Inc., Chino Hills, USA.

For cloning pUASattB-Kaede.*ptp69D$^{3'UTR}$*, the plasmid Kaede-N1 was obtained from Addgene (#54726). A recognition site for XhoI was inserted via site-directed mutagenesis of the XbaI site with the primers 5′-GCGGCCGCGACTCGAGATCATAATCAG and 5′-CTGATTATGATCTCGAGTCGCGGCCGC. The underlined nucleotide is the site of mutation in the XbaI recognition sequence (TCTAGA), creating the XhoI site (CTCGAG). The Kaede coding sequence was then excised with EcoRI and XhoI. The plasmid pUASattB-*ptp69D.mCherry* (see above) was opened with EcoRI and XhoI, and the coding sequence of Kaede was ligated into this backbone. For cloning the plasmid pUASattB-Kaede.*SV40*, the EcoRI / XhoI Kaede CDS fragment was inserted into EcoRI / XhoI-opened pUASattB plasmid (Bischof et al., 2007). The transgenic lines were created by microinjection of

pUASattB-Kaede.*ptp69D*$^{3'UTR}$ and pUASattB-Kaede.*SV40* into embryos of genotype *y*$^{1}$*w*$^{67}$*c*$^{23}$*; P{CaryP}attP40;* at BestGene, Inc., Chino Hills, USA. All constructs were integrated site- specifically into the same landing platform (*P{CaryP}attP40*) to avoid differences in transcription levels between the transgenes.

The Msi.HA transgenic line was created by the FlyORF Zurich ORFeome project (Fly line ID F004549 at www.flyorf.ch) at the University of Zurich, Switzerland, according to Bischof et al., 2013.

### Immunostainings

VNCs or brains were dissected from adult flies or pupae in 1x phosphate-buffered saline (PBS). Samples were fixed for 1.5 hr at room temperature (r.t.) in 2% paraformaldehyde (PFA; Merck, catalog #8.18708.1000) in 1x PBS containing 0.1% Triton X-100 (Sigma-Aldrich, catalog #X100; PBST). After several rinses and 3 washes of 10 minutes in PBST, tissues were blocked in 5% non-fat dry milk (NFDM) in PBST ("block solution") for several hours or overnight (o.n.) at 4°C. Incubation in primary antibodies was performed o.n. at 4°C or for $\geq$ 2 hr at r.t in block solution. After several rinses and 3 washes of 20 minutes in PBST, samples were incubated in secondary antibodies o.n. at 4°C or for $\geq$ 2 hr at r.t in block solution. After several rinses and 3 washes of 20 minutes in PBST, samples were mounted in SlowFadeTM Diamond Antifade Mountant (Invitrogen, catalog #S36972). Imaging was done on an LSM710 (Zeiss, Germany), or an SP8 (Leica microsystems, Germany) confocal light scanning microscope. Images were processed (cropping, rotation, contrast adjustments to the whole image) using ImageJ / Fiji (Schindelin et al., 2012) and Adobe Photoshop. Following antibodies were used at the indicated concentrations. 1:20 rat monoclonal anti-NCad DN-Ex #8 (DSHB); 1:1000 mouse monoclonal anti-GFP (Abcam, catalog #ab1218), 1:1000 rabbit polyclonal anti-DsRed (Clontech, catalog #632496), 1:1000 anti-Musashi (Okano Lab). Alexa Fluor-coupled secondary antibodies (AF488, AF55, AF633; ThermoFisher) were used at concentrations of 1:1000 - 1:500.

### Electrophysiology

Electrophysiological recordings were done according to Wentzel et al. (2018). In short: sharp-electrode recordings were made from muscle 6 in abdominal segments 3 and 4 in third-instar larvae using an Axoclamp 900A amplifier (Molecular Devices). The extracellular HL3 solution contained (in mM): 70 NaCl, 5 KCl, 10 $MgCl_2$, 10 $NaHCO_3$, 115 sucrose, 5 trehalose, 0.4 $CaCl_2$. From each muscle cell, 30 AP-evoked EPSPs were recorded (stimulus duration, 2 ms) and averaged. More than 40 mEPSPs were recorded and averaged for each cell to obtain the average mEPSP amplitude. Electrophysiology data were acquired with Clampex (Axon CNS, Molecular Devices) and analyzed with custom-written routines in Igor Pro (Wavemetrics).

### RNA fluorescence *in situ* hybridization (RNA-FISH)

Brains and ventral nerve cords from third instar larvae expressing Ptp69D.mCherry with an *elav*$^{C155}$*-Gal4* driver and from pupae at 48 hr apf expressing Ptp69D.mCherry with a *pnr-Gal4* driver were dissected in 1X Dulbecco's Phosphate Buffered Saline (PBS Sigma-Aldrich, catalog # D8537). Neuronal tissue was fixed in 4% parafolmaldehyde (PFA, Sigma-Aldrich, catalog #158127) for 1h at room temperature. After 3 washes of 5 min on ice in 1x PBS containing 0.1% Tween20 (Sigma-Aldrich, catalog #P9416 PBST), the tissue was dehydrated with 2 washes of 5 min on ice with Methanol (MeOH, Carlo Erba, catalog #414814). CNSs were stored overnight at −20°C. CNSs were rehydrated with 5 graded mixtures of MeOH/PBST washes of 5 min each on ice: (a) 75% MeOH / 25% PBST (b) 50% MeOH / 50% PBST (c) 25% MeOH / 75% PBST (d) 100% PBST (e) 100% PBST. CNSs were treated with 10 μg/mL Proteinase K for 2 min at room temperature. Post-fixation was done with 4% PFA for 20 min at room temperature, followed by 2 washes on ice with PBST for 5 min each. CNSs were washed 2 times with 50% PBST / 50% 5x Sodium chloride sodium citrate (Invitrogen, catalog #AM9770) with 0.1% tween (SSCT), and 2 times more with 5x SSCT for 5 min each on ice. CNSs were transferred to HCR hybridization buffer (Molecular Instruments) and incubated for 30 min at 37°C. CNSs were incubated overnight in HCR hybridization buffer with 4 nM of *mCherry* hybridization probe (Molecular Instruments, HCR 3.0, Choi et al., 2018; custom made). CNSs were washed 4 times with HCR probe wash buffer (Molecular Instruments) for 15 min at 37°C, and 2 times with 5x SSCT for 5 min at room temperature. CNSs were incubated for 5 min in amplification buffer at room temperature. Amplification was done overnight at room temperature in a dark box, with 30 pmol of each snap-cooled harpin h1 and harpin h2 prepared in 500 μL HCR amplification buffer (Molecular Instruments, HCR3.0, Choi et al., 2018). Samples were washed with 5X SSCT at room temperature, 2 times for 5 min, 2 times for 30 min and 1 time for 5 min. Samples were mounted in SlowFadeTM Diamond Antifade Mountant (Invitrogen, catalog #S36972). Imaging was done on an SP8 (Leica microsystems, Germany) confocal light scanning microscope. Images were processed using ImageJ / Fiji and Adobe Photoshop.

### Sample preparation for TRIBE

Neuronal expression of Msi.Adar$^{CD}$ and the constructs Ptp69D.mCherry, Kaede.ptp69D$^{3'UTR}$, and Kaede.SV40 was driven with *elav*$^{C155}$*-Gal4*. The amplification of *elav* 3′-UTR was done from flies expressing Ptp69D.mcherry. Amplification of *Dscam1* 3′-UTR was done from *Dscam1-Gal4* (GMR27G10) flies expressing Msi.Adar$^{CD}$. For the negative controls, the same drivers were used, without co-expression of Msi.Adar$^{CD}$. 10 third instar larvae were collected for each condition, and CNSs were dissected in RNAlater$^{TM}$ (Sigma #R0901). RNA was extracted using TRIzol® (Invitrogen #12183555). Traces of DNA in the samples were removed with DNA-free DNA removal kit (Invitrogen # AM1906). 100 ng of RNA were used to synthesize cDNA with the GoScript reverse transcriptase (Promega #A5003); RNAsin® (Promega, #N2515) was added to the reaction. cDNA was synthesized using specific primers for each construct as follows. (1) For the 3′-UTR from *Ptp69D.mcherry* and *Kaede.ptp69D*$^{3'-UTR}$: 5'-GAAACAATTCAAATCTGCTTA; (2)

for the CDS and 5′-UTR from *Ptp69.mcherry*: 5′-GTTGTGGGAGGTGATGTCC; (3) for *Kaede.SV40*: 5′-ACCTCTACAAATGTGG TATGGC; (4) for the isoform *ELAV-RB*: 5′-CGTGCTCGTTTATTAAGTATATAG; (5) for the isoform *ELAV-RD*: 5′-CTTAGGTCAA GAATTTATGC; (6) for the isoform *DSCAM1-RBD*: 5′-CATATATTTAGCAACTTATGAAC; and (7) for the isoform *DSCAM1-RCD*: 5′-CTAAGAAGGAGCGAGTGATTAG.

PCR amplification was done with Phusion® High-Fidelity DNA Polymerase (New England Biolabs #M0530). *Ptp69D* CDS and 5′-UTR were amplified using the primers: 5′-GCACTCGCCGCGACATTAG and 5′-GAAGCGCATGAACTCCTTGATG. Cycling conditions: initial denaturation 98°C 30 s; then 30 cycles of 98°C 10 s, 60°C 30sec, 72°C 2min 30 s; final extension 72°C 5 min. *Ptp69D* 3′-UTR from *Ptp69.mCherry* was amplified using the primers 5′-CATCAAGGAGTTCATGCGCTTC and 5′-CAATACACATAAAGGAA TACG. *Ptp69D* 3′-UTR from the *Kaede.ptp69D* 3′-UTR was amplified using the primers 5′-GATCAAGCTGCTTATGGAAGGC and 5′-CAATACACATAAAGGAATACG. *SV40* 3′-UTR was amplified from *Kaede.SV40* using the primers 5′-GATCAAGCTGCTTATG GAAGGC and 5′-ACCTCTACAAATGTGGTATGGC. *ELAV-RB* 3′-UTR was amplified using the primers5′-GGGCAATCGGGTGCTG CAGG and 5′-GCGCGATCCTCCTAATTGCCCC, *ELAV-RD* 3′-UTR was amplified using the primers 5′- GTTTGGCTTGATCAAA GAGCGCAGG and 5′-GGGTTGGGTCGGGTTTCCTAAGG, *Dscam1-RBD* 3′-UTR was amplified using the primers 5′-CGA AACCGGCCCAAAACAACTCC and 5′- GCGTATAACTCATGTTCAGAACGG, and *Dscam1-RCD* 3′-UTR was amplified using the primers 5′-CCGTTCTGAACATGAGTTATACGC and 5′-CTGCCTGTCCGCCTGGTTACAG. The same cycling conditions were used for all these 3′-UTRs: initial denaturation 98°C 30 s; then 30 cycles of 98°C 10 s, 60°C 30sec, 72°C 45sec; final extension 72°C 5 min. All PCR products were purified using 0.6X of AMPure XP (Beckman Coulter #A63880).

Libraries for PacBio sequencing were prepared at the Functional Genomics Center Zurich (FGCZ). Quality control of the amplicons was done with Qubit (Life Technologies, CA, USA) and Bioanalyzer (Agilent, CA, USA). The PCR products amplified from tissue expressing Ptp69D.mCherry corresponding to *Ptp69D* CDS and 5′-UTR, and the PCR product corresponding to the first replicate of *Ptp69D* 3′-UTR (shown in Figure S5A) were ligated to barcoded adaptors following the protocol "Procedure & Checklist - Preparing SMRTbellTM Libraries using PacBio® Barcoded Adapters for Multiplex SMRT® Sequencing v01" (Pacific Biosciences # 100-538-700-02) using the SMRTbell Template Prep Kit 1.0 (Pacific Biosciences #100-259-100) and SMRTbell Barcoded Adaptor Complete Prep-96 (Pacific Biosciences # 100-514-900). Each PCR product got a different barcode. A first pool was prepared from the PCR products corresponding to *Ptp69D* CDS and 5′-UTR with and without co-expression of Msi.Adar$^{CD}$. A second pool was prepared from the PCR products corresponding to the first replicate of *Ptp69D* 3′-UTR with and without co-expression of Msi.Adar$^{CD}$. The rest of the PCR products from tissue expressing Ptp69D.mCherry, Kaede.SV40, and Kaede.ptp69D$^{3'UTR}$ with and without co-expression of Msi.Adar$^{CD}$ corresponding to the second replicate of *Ptp69D* 3′-UTR, SV40 3′-UTR, *ELAV-RB* 3′-UTR, *ELAV-RD* 3′-UTR, *DSCAM1-RBD* 3′-UTR, and *DSCAM1-RCD* 3′-UTR (shown in Figures 5B and S5B–S5F) were ligated to barcoded overhang adaptors following the protocol "Procedure & Checklist - Preparing SMRTbell® Libraries using PacBio® Barcoded Overhang Adapters for Multiplexing Amplicons (Pacific Biosciences #101-791-700 version 04) using the SMRTbell Express Template Prep Kit 2.0 (Pacific Biosciences #100-938-900) and Barcoded Overhang Adapter Kit - 8A/8B (Pacific Biosciences #101-628-400/500). Each PCR product got a different barcode. After barcoding, a third pool was prepared by mixing equimolar concentrations of all PCR products. For each of the 3 pools, sequencing complexes were prepared by primer annealing to the library template and polymerase binding, using Sequel Binding and Internal Control Kit 3.0 (Pacific Biosciences #101-626-600). On the PacBio Sequel sequencing platform (Pacific Biosciences, Menlo Park, CA, USA), each pool was loaded to a SMRT Cell 1M v3 (Pacific Biosciences #101-531-000) and the Sequel Sequencing Kits 3.0 (Pacific Biosciences # 101-597-900) chemistry were used to sequence them.

### Real-time PCR

RNA from pupal heads at 48hrs apf, whole pupae at 48 hr apf, third instar larvae CNSs, and adult heads was extracted from wild-type (*w1118*) and *msi* null (*msi*[1]/Df(3R)*Exel6023*) flies. The same protocol for RNA extraction from samples for TRIBE was used. Three biological replicates were prepared for pupal heads, whole pupae, and adult heads. Two biological replicates were prepared for larval CNS. cDNA was synthesized with oligo(dT)18 primers, and random hexamers primers (Roche 05091284001). For cDNA synthesis of specific *ptp69D* 3′-UTR isoforms the following primers were used. (1) *Ptp69D* isoform 3: 5′-TTTTTTTTTATCAAGCTCATAAAAAG; (2) *Ptp69D* isoform 6: 5′-TTTTTTTTGAAACAATTCAAATCTG, (3) *Ptp69D* isoform 7: 5′-TTTTTTTTGGTTTCTATGTCAGGTTG. Quantitative qPCRs were performed with 3 technical replicates using MESA Green qPCR Mastermix Plus for SYBR® assay (Eurogentec #RT-SY2X-03+WOU) and an ABI Prism SDS 7900 HT system (Applied Biosystems, USA). Primer pairs for housekeeping genes and genes of interest were: *Actin* 5′-GCCCATCTACGAGGGTTATGC and 5′- AATCGCGACCAGCCAGATC (Toggweiler et al., 2016); *Tubulin-*$\alpha$ 5′-AGTCTCGCTGAAGAAGGTGTT and 5′- GCCAGATGCCGTCTGACAA (Toggweiler et al., 2016); *RpL32* 5′-TTGGGCATCAGA TACTGTCCC and 5′-GCAAGCCCAAGGGTATCGA (Poernbacher et al., 2012); *GAPDH* 5′- CTCCACCACATACTCGGCTC and 5′- TAAATTCGACTCGACTCACGGT (Wong et al., 2015); *Ptp69D* 5′-CGCGACAACGACGAAATTTG and 5′-CCGACAAAATGGGC AGTTCA.

### Protein-RNA co-immunoprecipitation

Protein-RNA immunoprecipitation without crosslinking was performed as follows. *Drosophila* embryos expressing Msi:HA with the *elav-gal4*$^{C155}$ driver, or without Msi:HA expression (controls, *elav-gal4*$^{C155}$ driver alone), were collected on apple juice agar plates. Embryos were dechorionated using 7% bleach for 5 min. After extensive washes, embryos were transferred to lysis buffer containing 50 mM Tris-HCl pH 7.5 (Biosolve Chimie #0020092391BS), 100 mM NaCl (SIGMA #71380), 1% Triton X-100 (SIGMA #X100), 0.1%

SDS (Thermo Scientific # 28312), 10% Glycerol (SIGMA # G7757), 5 mM MgCl2 (SIGMA #M2670), 1 mM EDTA (Fluka #03779), 1X cOmplete Mini protein inhibitor cocktail tablets (Roche #11836170001), and 100 U/mL of Recombinant RNasin ribonuclease inhibitor (Promega # N2515), and ground with a plastic pestle controlled by a motor grinder (Kimble Kontes #749540-0000). Samples were incubated 30 min on ice. The lysate was then centrifuged for 10 min at 4°C and 12000 g. 10 μg/mL of anti-HA antibody (BioLegend #901501) was diluted in a buffer containing 20 mM Tris-HCl pH 7.5, 100 mM NaCl, 10% Glycerol, 1 mM EDTA, and 5 mM MgCl2. A 1:1 mixture of lysate and antibody solution was mixed and incubated for 1 h at 4°C in a rotating wheel (5 μg/mL final concentration of anti-HA antibody). In the meantime, protein G Sepharose 4 Fast Flow beads (GE Healthcare #17-0618-01) were blocked for 1 h with BSA in lysis buffer at a concentration of 200 μg/mL, supplemented with 200 mg/ml of tRNAs. After blocking, the lysates were added to the Sepharose beads. Samples were incubated for 2 hr at 4°C. Beads were washed 3X with a buffer containing 20 mM Tris-HCl pH 7.5, 200 mM NaCl, 0.2% Triton X-100, 10% Glycerol, 1 mM EDTA, 5 mM MgCl2. RNA was extracted with TRIzol® (Invitrogen #12183555). The same protocol for cDNA preparation as for samples for TRIBE (see above) was used. Oligo(dT)18 primers were used to synthesize cDNA. mRNA was measured by qRT-PCR using the primers and the conditions indicated in the previous section. The primer pairs used for the additional genes tested were: *tramtrack*, 5′-CAACACCTGAAGGCACACAA and 5′-CCGAGTAGGGCACATCCTTA; *tata-binding protein*, 5′- CGCGCATCATCCAAAAGC *and* 5′- GCCGACCATGTTTTGAATCTTAA (Toggweiler et al., 2016). The enrichment of the indicated RNAs is shown upon normalization both to the input and to the mock IP.

Protein-RNA immunoprecipitation with crosslinking was performed according to Carrasco et al. (2020). Samples were collected from adult flies of 2 different genotypes: 1) *w1118*; 2) flies expressing Msi:HA with the *elav-gal4*$^{C155}$ driver. Material was collected as described in Carrasco et al. (2020). Specifically, adult flies were flash-frozen in liquid nitrogen, and 200 heads were hand-picked for each experimental condition. Crosslinking and lysis were performed as in Carrasco et al. (2020). 20 μg/mL of anti-HA antibody (BioLegend #901501), or a 1:10 dilution of hybridoma supernatant containing anti-Msi antibody (Hirota et al., 1999) were then added to the lysate. For the mock (control) IP with *w1118* extracts, 20 μg/mL of purified rat IgG isotype control was used (Invitrogen #02-9602). The mixture was incubated for 4 hr in a rotating wheel at 4°C. 80 μL of Protein G Sepharose 4 Fast Flow beads slurry (GE Healthcare #17-0618-01) were added to 1 mL of the lysate mixture and incubated for 1 h in a rotating wheel at 4°C. Beads were washed as described in Carrasco et al. (2020). RNA was eluted from the beads by Proteinase K treatment according to standard protocols (Worpenberg et al., 2021). RNA was extracted using TRIzol®. The same protocol for cDNA preparation as for samples for TRIBE (see above) was used. Random hexamers primers were used to synthesize cDNA. mRNA was measured by qRT-PCR using primers and conditions indicated above. The enrichment of the indicated RNAs is shown upon normalization both to input and to mock IP.

### Single-stranded DNA splint-mediated ligation assay to quantify poly(A) tails

25 pupal heads at 48 hr apf were collected from wild-type and *msi* null mutants by dissection in RNAlater (Sigma #R0901). RNA was extracted using TRIzol® (Invitrogen #12183555). RNA was ligated to an RNA anchor 5′- CAGCUGUAGCUAUGCGCACC GAGUCA GAUCAG-3′NH2 (Minasaki et al., 2014), with a modification in the 3′ end to ensure directional ligation. To increase ligation efficiency, a DNA splint 5′- CGCATAGCTACAGCTGTTTTTTTTT (Minasaki et al., 2014), was added to the reaction. In a 10 μL volume, 3 μg of RNA was annealed with DNA splint at a concentration of 2 μM and RNA anchor at a concentration of 3 μM. Incubation was done at 70°C for 5 min, 60°C for 5min, 42°C for 5min, and 25°C for 5min. The mixture was then ligated in a 20 μL volume containing T4 RNA ligase 2 (New England BioLabs #M0239S) and RNAsin®. DNA in the samples was removed with DNA-free DNA removal kit (Invitrogen # AM1906). 1 μg of RNA ligated to RNA anchor was used to synthesize cDNA with the GoScript reverse transcriptase (Promega #A5003) in a 20 μL volume with the reverse primer 5′-CTGATCTGAC TCGGTGCGCA (Minasaki et al., 2014).

Two different sequencing methods were used to quantify Poly(A) tails. To amplify the 3′-UTRs containing Poly(A) tails for Sanger sequencing, a nested PCR was performed for *Ptp69D*. For the alternative 3′-UTRs longer than 500 bp, a second nested PCR amplification was done with a primer that only binds to the distal 3′-UTR region present in the longer 3′-UTR isoforms. PCR amplification was done with GoTaq® G2 DNA Polymerase (Promega #M784B) in a 20 μL volume using 2 μL of the cDNA. Cycling conditions: initial denaturation 95°C 2 min; then 18 cycles of 95°C 25 s, 60°C 40 s, 72°C 30 s; final extension 72°C 5 min. 2 μL of this PCR product were used for the nested PCR using the same cycling conditions. For all PCR amplifications, the same reverse primers were used, these annealed to the RNA anchor sequence: first PCR, 5′- CTGATCTGACTCGGTGCGCA; nested PCR, 5′- TGCGCATAGCTA CAGCTGTTTT. For amplification of the *Ptp69D* proximal 3′-UTR region: first PCR, 5′-GAAGTGTGTCGACATCTGTGCC; nested PCR, 5′-CATAGCCGAGTCAACATTG. For amplification of the *Ptp69D* distal 3′-UTR region: first PCR, 5′-GAGCTTGA TAAGTGTGGTTTACATTC; nested PCR, 5′-GGTTGTGTGGATTAATGGTTTTCG. A 1:10 dilution of the PCR products was prepared and 2 μL of the dilution were used for TA cloning into the pSC-A-amp/Kan plasmid (Agilent Technologies #240205). Plasmid minipreps were done with PureYield Plasmid Miniprep System (Promega # A1223). 50 clones were sequenced by Sanger sequencing per condition, with some of them yielding poor sequencing reads.

To amplify the 3′-UTRs containing Poly(A) tails for PacBio sequencing, a nested PCR was performed for each gene of interest. For the genes with alternative 3′-UTRs that differ in length of more than 500 bp, two nested PCR amplifications were necessary to ensure that the proximal and distal 3′-UTR regions were amplified. PCR amplification was done with Phusion® High-Fidelity DNA Polymerase (New England Biolabs #M0530) in 20 μL volume using 2 μL of the cDNA template. The same cycling conditions were used for all 3′-UTRs: initial denaturation 98°C 2 min; and 18 cycles of 98°C 25 s, 60°C 25 s, 72°C 30 s; final extension 72°C 5 min. 2 μL of this PCR product were used for the nested PCR using the same cycling conditions. For all PCR amplifications, the same reverse primers were

used as for Sanger sequencing. For amplification of the *Ptp69D* proximal and distal 3′-UTR regions same primers were used as for Sanger sequencing. For the *Actin5C* proximal 3′-UTR region: first PCR 5′-GGATCGGGATGGTCTTGATTC; nested PCR 5′-GCATGTTGTGTGGTTCCAGCG. For the *Actin5C* distal 3′-UTR region: first PCR 5′-CCAACAACACCCAACACACG; nested PCR 5′-GTACAATTCGTCAGCAACC. For *GAPDH1* 3′-UTR region: first PCR 5′-CTATCGTACAAACCCGGCG; nested PCR 5′-GAAT CACTGTTGCATAATCCGC. For *GAPDH2* 3′-UTR region: first PCR 5′-CAAGAACACTACCCACCCAC; nested PCR 5′-GCTACTGTTTTCGCTCTTC. For *RpL32* 3′-UTR region: first PCR 5′-CAAGAAGTTCCTGGTGCAC; nested PCR 5′-CCAAGAAGCG CAAGGAGATTG. All PCR products were purified using 1.6X of AMPure XP (Beckman Coulter #A63880).

Libraries for PacBio sequencing were prepared at the Functional Genomics Center Zurich (FGCZ). Quality control of the amplicons was done with Qubit (Life Technologies, CA, USA) and Bioanalyzer (Agilent, CA, USA). Equimolar concentrations of each amplicon were mixed to prepare one pool for amplicons from wild-type and another one from *msi* null mutant. Each pool was ligated to barcoded adaptors following the protocol ''Procedure & Checklist – Amplification of Full-Length 16S Gene with Barcoded Primers for Multiplexed SMRTbell® Library Preparation and Sequencing'' (Pacific Biosciences #101-599-700 Version 03), with the modification that amplicons were ligated to barcoded overhang adapters instead of Overhang Adaptor v3. The SMRTbell Express Template Prep Kit 2.0 (Pacific Biosciences #100-938-900) and Barcoded Overhang Adaptor Kit - 8A/8B (Pacific Biosciences #101-628-400/500) were used. After barcoding, both pools were mixed and sequencing complexes were prepared by primer annealing to the library template and polymerase binding, using Sequel Binding and Internal Control Kit 3.0 (Pacific Biosciences #101-626-600). The PacBio Sequel sequencing platform (Pacific Biosciences, Menlo Park, CA, USA) with SMRT Cell 1M v3 (Pacific Biosciences #101-531-000) and the Sequel Sequencing Kits 3.0 (Pacific Biosciences # 101-597-900) chemistry were used.

### Western blotting

Polyacrylamide gels for separation of proteins, and western blotting to nitrocellulose membranes was done according to standard procedures. For the western blot shown in Figure S6, extracts were prepared from whole pupae, and 20 μg of protein were loaded per lane. A gel was prepared with a 10% final acrylamide concentration (Bio-Rad Laboratories, Inc. # 161-0156). For the western blot shown in Figure 6E, Mini-PROTEAN TGX stain-free gels (Bio-Rad Laboratories, Inc. # 4568033) were used. Proteins were transferred to Amersham Hybond P 0.45 PVDF membranes (GE Healthcare Life science #10600023), and incubated in following primary antibodies: 1:5000 anti-Actin (Abcam #ab3280), 1:1000 mouse monoclonal anti-beta Tubulin (DSHB #E7), 1:250 anti-Ptp69D (DSHB #3F11), 1:1000 anti-Robo1 (DSHB), 1:1000 anti-Musashi (Okano Lab), 1:000 anti-Lamin (DSHB # ADL67.10). HRP-conjugated secondary antibodies against mouse and rat, respectively (Jackson ImmunoResearch, #715-035-150 and 712-035-153) were used at a concentration of 1:5000. Chemiluminescence was generated with Amersham ECL Western Blotting detection reagents (GE Healthcare Life science #RPN2232) and detected on a Fusion Imaging system (Vilber, Germany).

### Prediction of 3′ UTR folding

RNA sequences were folded with RNAfold from the Vienna RNA websuite (Gruber et al., 2008; Lorenz et al., 2011). Another RNA folding server (RNAstructure; Reuter and Mathews, 2010) was used to confirm the result, and ProbKnot (Bellaousov and Mathews, 2010) was used to predict presence of pseudoknots.

## QUANTIFICATION AND STATISTICAL ANALYSIS

Data are expressed as mean ± standard deviation (SD), or mean ± standard error of the mean (SEM) in the bar graphs; details can be found in the figure legends. For the boxplots, the details of the depicted percentiles can be found in the figure legends. Statistical comparisons were performed using either a parametric unpaired t test, an unpaired t test with Welch's correction, a non-parametric Mann-Whitney test, a non-parametric Kruskal Wallis test, or a Pearson Chi-square test. A p value $< 0.05$ was considered significant. All statistical tests were performed with Prism 8 software version 8.0.2 (GraphPad). Details of all statistical tests can be found in the figure legends, including the p values. The number of samples (N, n) is depicted in each figure panel or figure legend. For Figures 1, , 2, 3, S1, S2, and S3, ''N'' refers to the number of animals analyzed. For Figure 4, ''N'' refers to the number of antennal lobes analyzed (2 per animal). For Figure S4, ''N'' refers to the number of neuromuscular junctions analyzed. For Figures 5, 6B–6D, S6E, and S6F ''n'' refers to the number of molecules sequenced. For Figures 6E, S5G, S6A, S6B, and S6G, ''n'' refers to the number of technical replicates from each biological replicate. For Figure S6D, ''N'' refers to the number of clones sequenced.

### Quantification of Synaptotagmin1 puncta

In Imaris software (Bitplane, an Oxford Instruments company; version 9.5.1), reconstructions were done for the Cherry.Syt1 channel using the Surfaces function. Smoothing was applied with a surfaces detail value of 0,277 μm. Background subtraction (local contrast) was used for thresholding, with the diameter of the largest sphere which fits into the object set at 0,7 – 1,04 μm. The thresholding value was set manually and individually for each image stack. Touching objects were split, with a seed point diameter value of 0.5 μm. This resulted in the number of Syt1 puncta, which were individually read for each MSN primary branch.

### Phenotype quantification

Confocal image datasets obtained from samples of flies of different genotypes were randomized. A second, blinded person without information of the genotypes manually classified the phenotypes. For the contralateral branch, following categories were scored: normal, loss of arborizations, midline or ipsilateral stop, and branch loss. For the posterior ipsilateral branch, the categories were divided into normal and presence of ectopic synapses, respectively. For the olfactory receptor neurons, the categories were normal, mild mistargeting, and moderate mistargeting.

Quantification of Brp area in individual glomeruli was performed in Fiji / ImageJ as following. First, signal was segmented to a binary image by using a threshold determined based on background signal. Brp area was determined based on the number of pixels above threshold in the correctly targeted and incorrectly targeted glomeruli, respectively. Brp area in the correct glomerulus was divided by the total Brp area to obtain the values shown in Figure 4N.

### RNA editing analysis for TRIBE

PacBio CCS (circular consensus sequencing) reads were generated and de-multiplexed to corresponding samples using the CCS Demultiplexing app in PacBio's open-source SMRT Analysis software suite SMRT Link (version 7.0.1.66975) with more stringent parameter settings than defaults (–minPasses 5–minPredictedAccuracy 0.999). CCS reads were aligned to the template sequence using minimap2 (Li, 2018, version 2.15r905) with the PacBio CCS preset parameter "-ax asm20." Variant calling was performed using lofreq (Wilm et al., 2012; version 2.1.2). At specific edited sites, allelic reads were extracted using customized job scripts, combining the utility script splitSNP (https://github.com/astatham/splitSNP), samtools (Li et al., 2009; version 1.3.1), and seqtk (version 1.2-r102; https://github.com/lh3/seqtk). Distribution of edited haplotypes among samples was analyzed in R (R Development Core Team, 2013).

### Real-time PCR

RNA fold change levels were calculated with the ΔΔCt method. In short, *ptp69D* mRNA levels were first normalized to the average Ct values of the housekeeping genes obtained from cDNA prepared with Oligo(dT)18 primers. *ptp69D* mRNA levels from the *msi* null mutant were then normalized to the mRNA levels in the control. Fold change levels were obtained by calculating $2^{-\Delta\Delta Ct}$. RNA fold change levels for specific *ptp69D* 3′-UTR isoforms were calculated by normalizing the Ct values of each *ptp69D 3′-UTR* isoform to housekeeping genes. In a second step, levels were normalized to the *ptp69D* mRNA total levels obtained from cDNA with random hexamer primers. To compare different developmental stages, all data points were normalized to the data point with the lowest mRNA level. Graphs represent the average and standard deviation of biological replicates.

RNA fold change after immunoprecipitation was calculated with the ΔΔCt method. For each gene the average ct value in each IP fraction (IP and mock IP) was normalized to the average Ct value of the corresponding input. Then the resulting ΔCt value of the anti-HA or anti-Msi IP was normalized to the corresponding average ΔCt value of the mock IP. Fold change levels were obtained by calculating $2^{-\Delta\Delta Ct}$.

### Quantification of poly(A) tail length

Two different sequencing methods were used to quantify Poly (A) tails. Samples sequenced by Sanger were manually analyzed. Poly(A) tails were measured between the last nucleotide that aligns to the reference genome sequence, and the sequence of the RNA anchor. Only samples where the RNA anchor sequence is present were used for the analysis.

Samples sequenced by PacBio were analyzed using a pipeline developed at FGCZ. In detail, PacBio CCS reads were generated and de-multiplexed to corresponding samples using the Auto CCS Demultiplexing app in SMRT Link (version 7.0.1.66975) with default parameters. Adaptor "CAGCTGTAGCTATGCGCA" on the 3′ end was trimmed using cutadapt (version 2.9; (Martin, 2011). Both the original read and its reverse complement were searched for the adaptor sequence. At least a 9 bases match between the adaptor and read was required for trimming. Reads without a matched adaptor were excluded from downstream analysis. Poly(A) tails in adaptor trimmed reads were first identified and trimmed using cutadapt (version 2.9) with a stringent maximum error rate of 0.01 (default 0.1). Reads, both poly(A) trimmed and untrimmed, were then mapped to dmel_r6.32_FB2020_01 gene sequences (ftp://ftp.flybase.net/genomes/Drosophila_melanogaster/dmel_r6.32_FB2020_01/fasta/) using the split aligner blat (Kent, 2002; v. 36x1) to identify any remaining poly(A) tails as unaligned tails on the 3′ end. If the unaligned tail had 90% and above of A bases, or if the unaligned tail was between 3 to 10 nt long and had only 1 none-A base, it was classified as part of the poly(A) tail and combined with the poly(A) tail identified by cutadapt, if there was one. If no poly(A) tail was identified by either of the two methods, the read was dropped from the analysis.

For each gene, poly(A) tail start sites in the gene sequence were used to group reads into isoforms. First, local maximas in the histogram of ploy(A) tail start sites were identified using R function "peaks" (R Development Core Team, 2013). A peak was defined as an element in the histogram which was greater than all other elements within a window of width span (25) centered at that element, meaning that a peak is the highest within a window of ± 12 bases. After all peaks were identified, each peak span was adjusted by distance to neighboring peaks (12 bases, or half of the distance to neighboring peaks, whichever was smaller). Refined peak spans were then used to classify reads into isoforms.

### Western blot quantification

Images were analyzed with the gel analyzer tool from Fiji / ImageJ. Signal from Ptp69D of pupal heads extracts was normalized to Lamin signal. Signals from Ptp69D and Robo1 of whole pupae extracts were normalized to Actin signal. Graphs show individual data points from western blots of 2 and 3 biological replicates of pupal heads and whole pupae, respectively.